IVYSPRING INTERNATIONAL PUBLISHER

Theranostics

2027; 17(2): 787-817. doi: 10.7150/thno.144282

Review

Charge carrier regulation in piezocatalytic nanomedicine

Tong He[1,2*], Yuqi Wen[1,2*], Zhiyang Wang[1,2*], Ge Wang[1,2], Yining Liu[1,2], Zhiqun Bai[1], Zhiguang Chen[1] ✉

1. Department of Ultrasound, The First Hospital of China Medical University, China.
2. Department of Second Clinical Medicine, China Medical University, China.

*Co-first authors and contributed equally to the conception and design of this study.

✉ Corresponding author: Zhiguang Chen, zgchen@cmu.edu.cn. Department of Ultrasound, The First Hospital of China Medical University, China.

© 2027 The Author(s). This is an open access article distributed under the Creative Commons Attribution 4.0 International Licence, subject to the Publisher's Terms of Use at https://ivyspring.com/terms.

Received: 2026.09.16; Accepted: 2026.10.23; Published: 2027.01.01

Abstract

Piezoelectric coefficients are critical parameters for assessing the performance of piezoelectric materials. However, the numerical values of these coefficients alone do not determine the catalytic activities of the respective materials. An important constraint on the output of piezocatalysis is the bulk electron-hole recombination process. This process has varying levels of severity dependent upon the relative ratio of the carrier diffusion length to the size of the material particles. Heterojunction engineering can decrease the effective carrier transport distance through the establishment of interfacial built-in electric fields. Defect engineering can extend the lifetime of carriers by providing them with shallow level trapping sites. Finally, piezoelectric hydrogels can alter the electrochemical environment at the interface through their continuous aqueous network. Using the conceptual framework described above, this review examines two novel fields of research - piezoelectric immunoengineering and two dimensional piezoelectric materials - and outlines a strategy for method selection using a decision tree developed specifically for clinical applications. This decision tree will guide selection of methods based upon the amount of ROS needed to achieve desired results, how deeply the target lesion is located, and whether or not long term implantations are needed. Throughout, this review continuously focuses on translating laboratory research into clinical practice. This review discusses several potential obstacles to translating laboratory research into clinical practice including issues related to *in vivo* retention toxicity, non-selective ROS oxidation, and a lack of standardized testing methods. Additionally, this review provides possible solutions for overcoming each of these challenges. Finally, this review develops a stepwise translational pathway that is based upon the format of the product being developed. Future work should include developing systematic comparisons of various methods, utilizing existing approved material platforms for translational studies, and designing new materials using data derived from previous translational studies.

Keywords: piezocatalysis; heterojunction engineering; defect engineering; piezoelectric hydrogels; clinical translation

1. Introduction

The limitations of systemic chemotherapy are related to the dosage applied to the patient. Long-term use of antibiotics will result in selection of resistant strains [1,2]. Reactive oxygen species (ROS)-mediated catalytic treatments provide a possible solution to the problem of tumor development of resistance to treatment. This is because ROS-mediated catalytic treatments have multiple target oxidative mechanisms, making it difficult for tumors to develop resistance via a single molecular pathway [3,4]. Some ROS therapies (e.g., chemodynamic therapy) take advantage of endogenous H_2O_2 and transition metal Fenton chemistry, without requiring an external energy source. However, the cell's internal redox homeostasis can offset exogenous ROS via its antioxidant defense systems. When external energy is required to deliver the ROS, the ability to penetrate the tissue determines whether the ROS will reach the intended area [3,5]. Photodynamic therapy demonstrates this limitation: visible light can only penetrate several millimeters into soft tissue, and near-infrared light is significantly scattered and attenuated within several centimeters [5]. Diagnostic ultrasound typically operates in the 1-5 MHz frequency range and

can routinely image structures located greater than 10 centimeters deep in soft tissue. Attenuation of ultrasound is dependent on frequency and is estimated at 0.5-1.0 dB/cm/MHz [6]. Thus, the primary limitation to effective delivery of the ROS becomes the ability to get the sonosensitizer to the area of interest. Organic porphyrin-based sonosensitizers are unstable under ultrasound exposure, and this limitation has motivated the exploration of inorganic piezoelectric sonosensitizers [4,7-9]. ROS generation from organic porphyrin-based sonosensitizers occurs through the highest occupied molecular orbital-lowest unoccupied molecular orbital (HOMO-LUMO) energy transfer framework: transient temperatures and sonoluminescence created by cavitation excite the sensitizer to either its singlet or triplet state. Following excitation, the sensitizer transfers its energy to molecular oxygen resulting in singlet oxygen or superoxide formation [5]. An alternative approach to generating ROS is through inorganic piezoelectric catalysts, which, unlike inorganic sonocatalysts (e.g., TiO_2) excited mainly by cavitation-derived hot spots and sonoluminescence, separate charges through the piezopotential generated by lattice deformation. Under ultrasonic alternating stress, non-centrosymmetric lattices become polarized. The resulting band bending causes electrons and holes to migrate to the surface of the catalyst to facilitate conversion of O_2 and H_2O into ROS [10-13]. Similar to photocatalysis, charge separation and transport mechanisms occur similarly in inorganic piezoelectric catalysis. The major difference between the two processes is the excitation source used [12,14,15]. Of the 32 crystallographic point groups, 21 are non-centrosymmetric, and 20 of these can demonstrate piezoelectric behavior. Therefore, piezoelectric behavior is symmetry dependent, rather than being a general characteristic of all crystal lattices. Many inorganic piezoelectric materials demonstrate excellent chemical stability and allow for wide variations in their composition, morphology, and defects. These characteristics create a large design space for biomedical applications [7,11,12].

Among the various material-level approaches to improving piezocatalytic performance, increasing the piezoelectric response has received the greatest emphasis [14,16]. The d_{33} value is a measure of the amount of charge that develops due to applied mechanical force; as such, it serves as the initial step in the stress–polarization–band-bending process [16,17]. An increase in d_{33} will result in a larger piezopotential developed when subjected to the same amount of mechanical force, thus resulting in increased band bending and a wider range of redox potentials that can be utilized for surface reactions [9,17-19]. Solid-solution designs and poling treatments to increase the d_{33} values of tetragonal-phase $BaTiO_3$ systems have been found to increase the overall piezocatalytic productivity of these systems [19-21].

While it is known that d_{33} directly influences carrier generation, there has been very little documentation regarding how d_{33} directly correlates to ROS production. d_{33} is simply the first step of many sequential processes that will ultimately determine catalytic efficiency. These steps include: carrier generation (which is determined by both d_{33} and the amount of stress applied), carrier migration and bulk recombination (which are determined by diffusion length, particle size, and defects present), surface recombination, and surface reaction rates [16,22-25]. The lifetime of carriers produced in oxide semiconductors varies from nanoseconds to microseconds, allowing for diffusion distances of a few nanometers to greater than 100 nanometers. Many commonly used piezocatalysts have particle dimensions ranging from about one hundred nanometers to several micrometers [21,26,27]. When the diffusion length of a carrier is significantly smaller than the particle size of the material, only carriers generated close to the surface can successfully migrate to the surface to participate in reactions. All other carriers generate and recombine within the bulk of the material. Therefore, bulk recombination is a major limiting factor for overall efficiency, along with many other factors such as ultrasonic parameters, surface reaction rates, and the biological environment, and research focuses on optimizing the use of generated carriers rather than increasing the number generated.

This restriction can be resolved by using three different but related material design techniques. Heterojunction design is used for the spatial aspects of materials: an internal electric field that exists as a result of differences in work functions and band alignments of two different phases causes electrons and holes to move in opposite directions. This movement shifts the location of the charge separation process from inside the bulk material to near the interface of the two phases, thereby decreasing the overall distance that charges must travel [24,28,29]. How much the distance is decreased depends upon how the interface is designed; for example, if the heterojunction is a core-shell structure, then the charge transport distance is reduced from the size of the particle (radius) to the thickness of the outer shell. If the heterojunction has a planar or random-contact design, then the size of the space-charge region determines how much the charge transport distance will be reduced. Defect design addresses the temporal aspects of materials: defect designs include oxygen vacancies, cation vacancies, and other defects (aliovalent dopants) that produce

localized state levels within the energy gap. These state levels can capture charges and then release them after some amount of time (nanoseconds to milliseconds). Therefore, defect designs increase the amount of time that charges remain active, which increases the probability that they will reach the surface [25,30,31]. Piezoelectric hydrogels address the catalyst medium aspects of materials: because the hydrogels have high ionic conductivities due to being made up of a large number of interconnected water channels, the piezoelectric fields developed within the hydrogels can interact directly with the electrochemical processes taking place at the boundary between the solid and liquid components. This eliminates the need for long-range charge transport within the solid component [32-34]. All three techniques do not necessarily have to be employed separately. Defects often develop at heterojunction boundaries, and piezoelectric hydrogels can contain piezoelectric particles that have been altered using either defect design, interface engineering, or both [35-38].

This paper will examine how charge carriers are regulated in piezocatalytic nanomedicine through space, time and catalytic medium (**Figure 1**) and extend this framework to two additional emerging areas: piezoelectric immunoengineering and 2D piezoelectric materials [39,40].

2. Core bottleneck: physical origins of electron–hole bulk recombination

Ultrasonic alternating stress results in periodic deformation of the piezoelectric semiconductor lattice, leading to the development of polarization charges and a piezopotential within the lattice [20,41]. Band bending causes the separation of electron-hole pairs and their subsequent migration in a specific direction. The carriers that reach the surface are believed to participate in the oxygen reduction and water oxidation reactions at the surface of the material, generating ROS[42,43]. The piezoelectric field along with the accompanying ionic migration may also provide physical stimuli, and in turn, influence and regulate the behavior of cells and assist in the repair of tissues [44]. The series of steps that include the generation of polarization charges, the transport of the carriers, and the surface reactions are subject to efficiency losses at each individual step, which ultimately limits the total catalytic process [26].

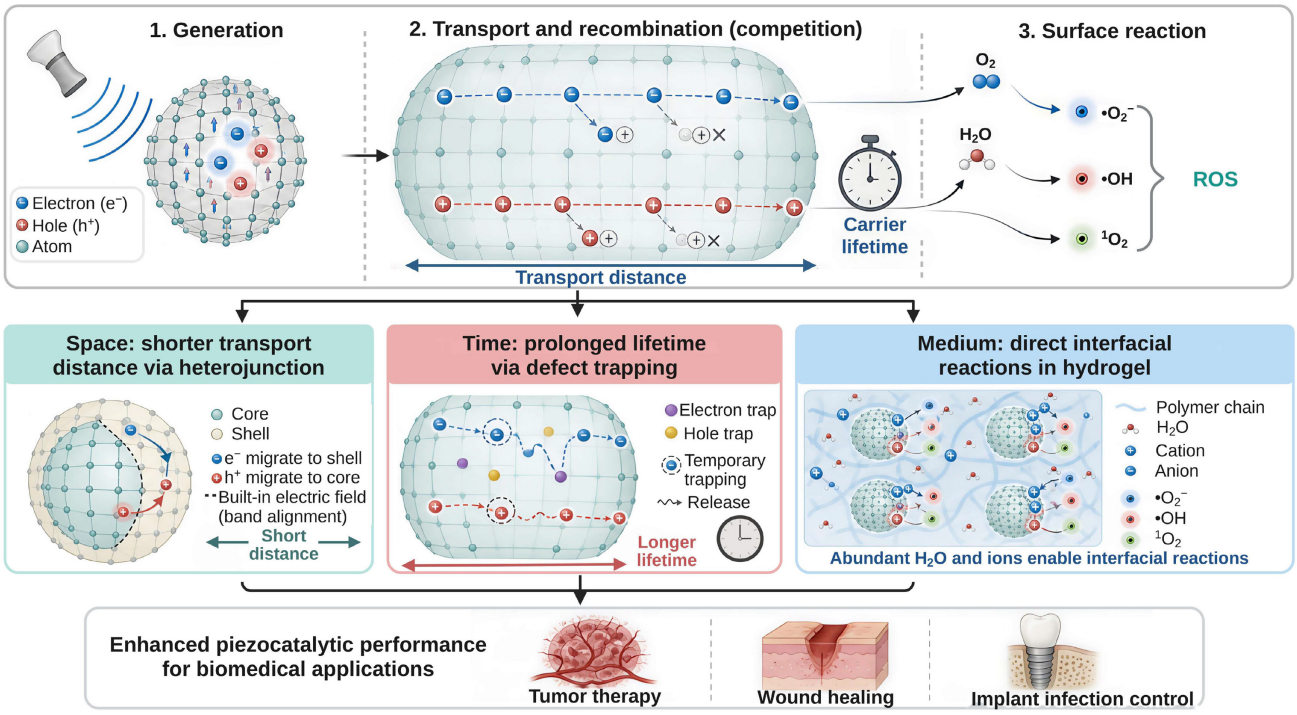


Figure 1. Regulatory framework of charge carriers for piezocatalytic nanomedicine. Upper panel: The three sequential processes that charge carriers experience when activated by ultrasound in piezoelectric materials, i.e., charge generation (1); charge transport vs. recombination competition (2); and charge reaction at the surface (3). The relative value of the charge carrier's transport distance to its lifetime defines how effectively it can be utilized. Lower panel: Three regulatory approaches to address the bulk recombination bottleneck. Spatial Approach (SPACE): Heterojunctions created by engineering shorten the effective distance for charge carrier transport due to an internal electric field generated at the interface; Temporal Approach (TIME): Defect engineering extends the effective lifetime of charge carriers by trapping them in shallow levels; Catalytic-Medium Approach (MEDIUM): Piezoelectric hydrogels create a continuous aqueous network which alters the interfacial electrochemical environment, thereby decreasing the reliance on long-distance charge carrier transport in the solid-phase. These three approaches collectively improve the efficiency of piezocatalysis, providing potential solutions for biomedical applications such as tumor therapy, wound healing, and implant infection control.*Created in BioRender. T. (2026) https://BioRender.com/ebziw4u.*

However, it should be noted that a greater d_{33} does not necessarily translate into a higher level of catalytic activity. While the effective d_{33} for O_v-BOS is comparable to that of the original control sample, O_v-BOS produces about 10 times more ROS [45]. Therefore, d_{33} is only one of many parameters contributing to the overall performance of a catalyst, and because ultrasound parameters and ROS detection methods differ across studies, d_{33} and ROS yield are compared here only within the same study.

The Piezoelectric Potential Drives Interfacial Reactions: A Theoretical Framework. There are two theoretical models which have been developed to describe the mechanism of how piezoelectric potential can lead to interfacial reactions. The first model is the energy band model which will be used in this article. The second model is the screening charge model [18,34]. In dilute aqueous solutions, the screening charge model is likely to be dominant due to the rapid compensation of surface polarization by mobile ions within the electric double layer. However, in solid state heterojunctions where both the built-in electric field and band offset remain intact across the interface, the band bending description is able to better account for the directional separation of carriers [46]. Although these models are fundamentally different from each other, they share a common limitation. Regardless of which model is responsible for initiating the reaction at the interface, only a small percentage of the generated charges can reach the reactive interface because of recombination in the bulk when the diffusion length of carriers is shorter than the size of particles. Therefore, it is reasonable to treat bulk recombination as a central factor limiting the overall efficiency across mechanistically diverse systems, although there may be additional limitations imposed by such factors as ultrasound parameters, sonochemical contributions, surface reaction kinetics, and the biological environment.

Understanding the dynamics of carriers in photocatalysis provides useful insight into this issue. In TiO_2 and other oxide semiconductors, charge utilization efficiency is determined by the relationship between carrier diffusion length and particle size [25,28]. If the diffusion length is significantly smaller than the particle size, then the majority of charge carriers are generated in the bulk of the semiconductor and recombine before reaching the surface [27,47]. This is also true for piezocatalysis: diffusion lengths in semiconductors are on the order of a few nanometers to several hundred nanometers, while the size of typical piezoelectric catalysts is on the order of several hundred nanometers [8,27,48,49]. For systems where the diffusion length is in the lower range of this scale, then bulk recombination is the main limiting factor for catalytic efficiency.

There are three dimensions where bulk recombination can be reduced.

Spatial: shortening the distance carriers need to travel to reach the reactive interface. In a heterojunction, the band offset at the two-phase contact region, along with an interfacial built-in electric field, can facilitate the opposite directional transport of charge carriers. This process can fully separate the charge carriers near the interface, thus shortening the distance carriers need to travel from the radius of the particle to the thickness of the shell or the interfacial layer [50,51]. This is the reason for the catalytic enhancement of $BaTiO_3$@TiO_{2-x} core-shell heterojunctions [35] and the chemically bonded heterojunctions of $BaTiO_3$ and MoS_2 [52], both observed under combined light and ultrasound. Heterojunctions such as $BiFeO_3$@CdS nanofibers and CuS/ZnO Z-scheme composites also show enhanced piezocatalytic activity under ultrasound alone [53,54].

Temporal: extending survival time of the carriers prior to recombination. Oxygen vacancies, cation vacancies, and aliovalent doping introduce discrete energy levels in the bandgap, which creates a potential energy well. Carriers become trapped in the well and are later released, thus lowering the chance of direct recombination and increasing effective lifetimes [55]. Charge trapping and release mechanisms are believed to explain the enhanced ROS generation observed with O_v-BOS nanosheets [45]. There is an optimal range for the depth and concentration of defect energy levels [56]. If defect energy levels are too deep or too many, they convert to nonradiative recombination centers, which then increases carrier losses [39,57].

The Catalytic Medium Dimension: Reducing Dependence on Solid Phase Long Range Carrier Transport. The continuously connected three dimensional aqueous channels in piezoelectric hydrogels facilitate direct interaction between the piezoelectric field and the polarization of water molecules, as well as the electrochemical reduction of dissolved oxygen. The presence of the aqueous medium changes the ionic conductivity of the nearby area, as well as the manner in which polarization charges are involved in chemical reactions. Specifically, polarization charges produced at the surface of the piezoelectric particle are immediately neutralized and balanced out by hydrated ions present in the aqueous phase, resulting in the formation of an electrical double layer. This process bypasses the reliance upon solid phase bulk transport, where losses can be very high [58,59]. We use the term "catalytic medium dimension" to indicate that the hydrogel alters the ionic environment around the piezoelectric phase and the electrochemical interface of the

piezoelectric phase, as opposed to modifying carrier dynamics in the solid state material itself.

Heterojunction engineering, defect engineering, and piezoelectric hydrogels engineering are the three pathways identified in the subsequent sections. In engineering the same system, the three strategies can be integrated. Hydrogels can contain piezoelectric materials that have been modified by defect engineering, interface engineering, or both [35,60].

3. Strategy I: heterojunction engineering and spatial-dimension charge separation

3.1 Heterojunction configurations and charge carrier separation mechanisms

Heterojunctions shift the location of charge carrier separation to the interface region of a given phase, which is the main strategy to limit the recombination of charge carriers within a given phase. At the contact of two different phases, the differences in work function and the Fermi level initiate imbalances in the interfacial charge, which results in a space charge region with band bending and an interfacial built-in electric field [61]. The application of ultrasound produces a periodic change of geometry in the piezoelectric phase, which leads to the formation of an alternating piezopotential [62]. During a given stress cycle, if the piezopotential is in the same direction as the interfacial electric field, the field enhances the directional movement of the charge carriers, thereby reducing the distance of transport from a particle scale to the region of the interface [63].

Heterojunctions can either be classified as semiconductor-semiconductor or semiconductor-metal junctions based on the second component and the separation mechanisms employed. It is predominant for semiconductor-semiconductor junctions to rely on the band offset to facilitate the unidirectional mobility of carriers. Reported piezocatalytic semiconductor heterojunctions consist of Type-I and Type-II band configurations, Z-scheme and S-scheme charge transfer pathways, and p-n heterojunctions [61,64,65]. This study has chosen Type-II and S-scheme heterojunctions to outline the distinctions between the two types with regard to the spatial carrier separation as well as the preservation of the redox [66,67]. Type-II heterojunctions are capable of accumulating majority carriers while maintaining carrier separation; however, this can concurrently weaken the oxygen reduction and the water oxidation capability [68]. S-scheme heterojunctions are able to maintain the separation of the conduction band and the valence band holes, thus retaining the energy balance and the strong driving force and therefore are more attractive for applications in piezocatalytic systems.

The mechanism of separating charge carriers at a semiconductor-metal junction is quite different than the band offset mechanism presented previously. A metal with a very high work function will allow for electrons to move into the metal from an n-type piezoelectric semiconductor until the Fermi levels on both sides equilibrate. At this point, the semiconductor will develop a depletion region and a Schottky barrier at the junction. Most piezoelectric semiconductor systems have only one type of carrier that contributes to their electrical conductivity. For n-type piezoelectric materials, the Schottky barrier prevents electrons from moving from the metal back into the semiconductor, which minimizes the amount of electron-hole recombination occurring at the junction. Some representative examples of these types of systems are the $Ti_3C_2T_x/MoS_2$ system, where $Ti_3C_2T_x$ is a metal acting as a sink for electrons and forms a Schottky contact with MoS_2 (a semiconductor) [69]; and the $AgNbO_3$/Pt system, where platinum captures electrons at the junction and also exhibits catalase-like activity to break down endogenous H_2O_2 [70]. Both systems utilize the metal component as a one-way electron reservoir and the Schottky barrier as a permanent built-in asymmetry during the application of ultrasonic stress.

The three types of representative heterojunctions are shown to exhibit various types of band alignments and different pathways for carrier migrations (Figure 2). However, in the Schottky and S-scheme configurations, only one of the two materials exhibits the property of piezoelectricity. Therefore, by employing only one of the materials, the process of optimizing the interface electric fields and piezoelectric fields may be optimized [71,72].

3.2 Validation of interface structure on separation efficiency

The preceding categorization provides insight into the various configurations of heterojunctions. The next pertinent question is whether the design of heterojunction interface can enhance the efficiency of carrier separation. There is relatively clear empirical evidence from the $BaTiO_3@TiO_2$ core-shell system. Liu et al. [29] created $BaTiO_3@TiO_2$ nanowires within the zone of piezo-photocatalysis with $BaTiO_3$ as the piezoelectric core, and TiO_2 as the continuous shell. The heterojunction interface enhanced the carrier concentration from 2.28×10^{17} cm^{-3} to 4.91×10^{18} cm^{-3}, improved the electron lifetime derived from impedance (Bode) analysis from 50.37 ms to 60.98 ms, and achieved near-complete degradation of the high concentration dye in a piezo-photocatalysis system. Further, Wang et al. [35] synthesized a core-shell

heterojunction system of $BaTiO_3$@TiO_{2-x} via a one-step hydrothermal route with Ti^{3+} and created oxygen vacancies at the core-shell interface. After 80 min of synergistic light and ultrasound treatment, the system achieved 99.01% removal of Rhodamine B, with an apparent rate constant of 5.39×10^{-2} min^{-1}, which is ca. 7.8 times more efficient than the unmodified $BaTiO_3$. From the perspective of heterojunction design, the continuous core-shell interface set a specific path for charge carrier migration, with piezoelectric polarization continuously adjusting the interfacial band. The synergism of the two phenomena reduced the distance for carrier transport [29]. The role of the oxygen vacancies in improving both the light absorption process and the carrier dynamics will be analyzed in greater depth in Section 4, within the context of defect engineering. Together, these two studies demonstrate that continuous core-shell interfaces can significantly reduce carrier transport distances, shifting charge separation pathway from the bulk to the region adjacent to the interface.

While the core-shell system shows that interfacial design can decrease transport distances, the efficiency of separation is also dependent on the quality of bonding at the interface.

Han et al. [52] constructed an integrally bonded $BaTiO_3$/MoS_2 dual-piezoelectric heterojunction and described its interfacial electronic structure using density functional theory integrated with spectroscopic analysis. Based on the calculations, the 3d orbitals of Ti in $BaTiO_3$ and the 3p orbitals of S in MoS_2 form stable chemical bonds that lock $BaTiO_3$ on the 2D surface of MoS_2. Close proximity allows the transfer of charge from $BaTiO_3$ to MoS_2. $BaTiO_3$ and MoS_2 then reach equilibrium of their respective Fermi energies, establishing a Type-II band alignment with an interfacial built-in electric field. When both light and ultrasound are applied, the conduction and

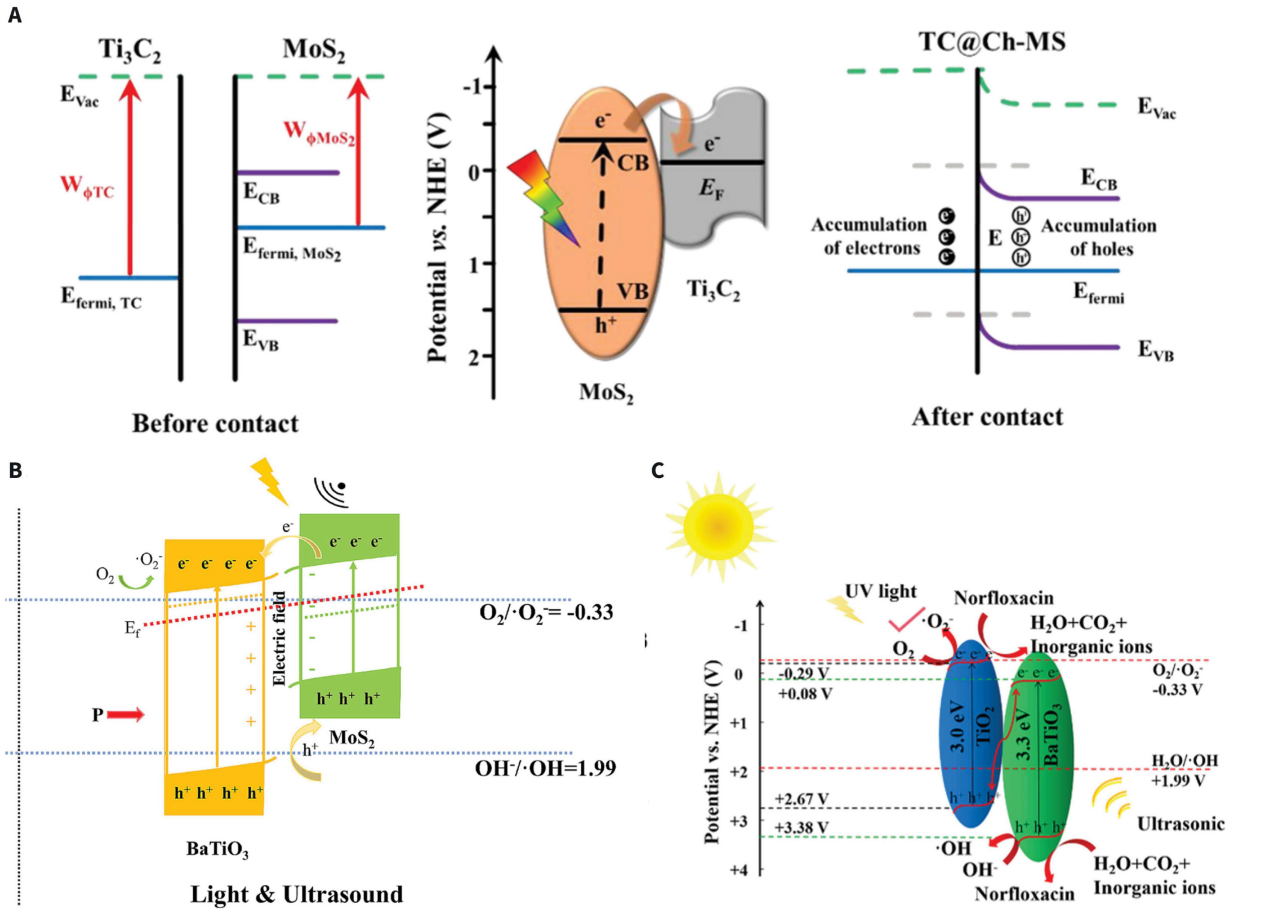


Figure 2. Band alignments and charge transfer pathways of three representative heterojunction types in piezocatalysis and piezo-photocatalysis. (A) Schottky heterojunction of $Ti_3C_2T_x$ and MoS_2. Both $Ti_3C_2T_x$ as a metal and MoS_2 as a semiconductor have different Fermi levels prior to being in contact. Once they are in contact, the interfacial charge redistribution will produce a Schottky barrier. The electrons in the MoS_2 can move into the $Ti_3C_2T_x$ where they will be accumulated on the metal side. The Schottky barrier prevents the electrons from flowing back into the MoS_2. Furthermore, the ultrasound-induced piezoelectric polarization can further promote the separation of the interfacial charges. Adapted with permission from Ref. [69]. Copyright 2022 Wiley-VCH GmbH. (B) $BaTiO_3$/MoS_2 Type-II heterojunction. When both light and ultrasound are present, electrons move from MoS_2 to the $BaTiO_3$ conduction band, and holes move from $BaTiO_3$ to the MoS_2 valence band. This creates an interfacial built-in electric field, which works together with the ultrasound-induced piezoelectric polarization to enhance spatial carrier separation. Adapted with permission from Ref. [52]. Copyright 2025 Elsevier Inc. (C) $BaTiO_3$/TiO_2 S-scheme heterojunction under combined light and ultrasound. The lower reducing ability electrons and lower oxidizing ability holes recombine at the heterojunction interface, which preserves high-reducing ability conduction band electrons and high-oxidizing ability valence band holes. Adapted with permission from Ref. [67]. Copyright 2022 Elsevier B.V.

valence bands of both materials are further tilted, the average electrostatic potential difference increases, and the carrier separation is intensified. The BM-10 sample demonstrated the best performance in the series. The design of BM-10's composition led to optimization, and is considered in comparison to other systems. Although a model catalytic reaction was the subject of this study, the findings are relevant to the design of biomaterials. The tradeoff between physical and chemical bonding is a balance of mixing and contact. Chemical bonding improves interfacial dipole, decreases cross-interface resistance, and preserves interfacial structure during cavitation from ultrasonic cycling.

The primary objective of designing a heterojunction for biomaterials is to enhance carrier transport while maintaining structural integrity. The choice of heterojunction determines the reactive species and whether they gather the target biomolecular interaction. In a representative environmental catalysis study, Zhao et al. [67] prepared S-scheme $BaTiO_3/TiO_2$ thin films that removed over 90% of norfloxacin under piezo-photocatalytic conditions within 60 minutes. This exhibited a pseudo-first order rate constant of 43×10^{-3} min^{-1}, which was 2.69 times greater than that of unmodified TiO_2. The main reactive species were identified to be holes and hydroxyl radicals. The S-scheme pathway is able to overcome some of the limitations of environmental catalysis as taming highly oxidizing holes is crucial to enhance catalysis. However, the most notable advance in tailoring heterojunction piezocatalysis for biomedical use is Zhang's work with $AgNbO_3$/Pt@HA [70]. Using only ultrasonic energy, Zhang's work showed that $AgNbO_3$ catalyzed piezo-splitting of water to generate H_2 and hydroxyl radicals, while platinum catalyzed the formation of a Schottky interface and exhibited catalase like activity to decompose endogenous H_2O_2 to provide O_2. This work showed an almost 50% reduction in tumor interstitial fluid pressure, 59.4% of tumor associated fibroblasts underwent apoptosis, and a 44.07% reduction in tumor solid stress. This also showed that physical barriers were relieved of their restrictions, there was a positive shift in the balance of the immune system of the body with an increase in the numbers of $CD8^+$ and $CD4^+$ T cells of 3.95- and 3.00-fold, respectively, and that there was a change of macrophages from M2 to M1 in addition to immunogenic cell death and the polarization of macrophages as a result. Using ultrasound to initiate therapy with the MoS_2/MXene atomic-thin-layer Schottky heterojunction also showed that two dimensional interfaces can provide a transport pathway that is shorter, flexible, and an electron sink and simultaneous nanozyme activity. The driving conditions, evaluation targets, and key performance indicators of the above systems are summarized in **Table 1.**

Most of the interface evidence above comes from piezo-photocatalytic tests, whereas deep-tissue therapy relies on ultrasound alone, and the two excitation modes supply carriers in different ways. Under illumination, above-bandgap photons generate electron-hole pairs throughout the absorbing volume, and the piezopotential acts mainly as an additional field that tilts the bands and steers these photogenerated carriers apart. Under pure mechanical stress, interband excitation is absent apart from cavitation-derived sonoluminescence, which belongs to the sonochemical pathway. The reactive charges come from intrinsic and defect-derived free carriers and from the screening charges that compensate the polarization, and the piezopotential itself has to bend the bands far enough for these charges to reach the redox levels of O_2 and H_2O [18,34]. This band bending rises and falls with every stress cycle, so the carrier supply is intermittent and far smaller than under continuous illumination. The light-assisted studies therefore establish how interface continuity, chemical bonding, and band alignment direct carrier flow, and these design principles carry over to ultrasound-only systems, whereas their degradation rate constants cannot be read as measures of *in vivo* piezocatalytic efficacy. Ultrasound-only evidence for heterojunction-mediated separation in a biological setting currently comes from the $AgNbO_3$/Pt and MoS_2/MXene Schottky systems [69,70], and Table 1 lists the driving condition of each entry.

3.3 Design principles and current limitations

Heterojunction design can be simplified into three design principles. First, core-shell structures and two-dimensional conformal contacts may yield greater effective interfaces with shorter transport distances compared to random mixing. The relationship between two-phase ratio and performance shows a volcano-type trend. In the $BaTiO_3/MoS_2$ system, BM-10, and in the n-TiO_2/$BaTiO_3$/p-TiO_2 system, TBT3, these heterojunctions outperformed systems with low and high loadings. In TBT3, carrier lifetime improved from 1.88 ns to 3.28 ns and improved from 43.6% to 86.6% separation efficiency; however, new outer layers of TiO_2 caused performance degradation due to particulate clustering and slowed transport across the interfaces. The optimal ratio of components is a balance of interfacial area, transportation, resistance, and agglomeration and must be determined experimentally. Second, interfaces should be constructed using *in situ* growth or chemical bonding

to stabilize the interfacial dipole, reduce resistance, and improve structural integrity under ultrasonic cyclic stress. Finally, design choice of the type of junction should be influenced by targeted ROS and the desired biological impact. For simultaneous preservation of oxidizing holes and reducing electrons, the S-scheme should be used; and for prevention of backflow of electrons, the Schottky type should be used.

Currently, the biggest challenge lies in the heterojunction interfaces. The amount of variability in interfacial trap density, local oxidation states, and charge-transfer efficiency phase composition from batch-to-batch is quite large and documented throughout the literature on the subject [36]. As soon as heterojunction nanoparticles are introduced into a biological system, the biological environment will introduce several levels of interference with the interfacial built-in electric field. Protein corona formation will coat the particle surface within seconds after being exposed to either blood or interstitial fluid. This adsorbed protein layer will change the surface charge and the effective dielectric constant at the interface [73]. In physiological saline (about 150 mM), the Debye length is only about 0.8 nm, so the electrostatic part of the built-in field is screened within the first nanometer of the surface. Zwitterionic coatings or PEGylation do not change the Debye length, which is set by ionic strength, but they can reduce nonspecific protein adsorption and may partly preserve the surface piezopotential. The majority of studies have used endpoint measurements of ROS to infer the efficacy of separation. By using this method, they were unable to assess how much interfacial charge transfer played a part. Future investigations should look toward *in situ* interfacial charge transfer measurements in liquid-phase and physiological-fluid systems.

Table 1. Summary of heterojunction evidence

Material System	Heterojunction Type	Driving Conditions	Evaluation Target	Key Performance Indicators	Interface/Mechanism Evidence	Reference
$BaTiO_3$@TiO_2 nanowires	Type-II core-shell heterojunction	Piezo-photocatalysis (45 kHz, 200 W)	Dye degradation	Carrier concentration $2.28\times10^{17}\rightarrow4.91\times10^{18}$ cm^{-3}; EIS-derived electron lifetime 50.37→60.98 ms; near-complete degradation in a high-concentration dye model	$BaTiO_3$ as the piezoelectric core, TiO_2 as the continuous shell; core-shell interface establishes a directional migration channel, shortening carrier transport distance	[29]
$BaTiO_3$@TiO_{2-x} core-shell heterojunction	Type-II core-shell heterojunction; with oxygen vacancies	Piezo-photocatalysis (40 kHz, 120 W)	RhB degradation	80 min removal rate 99.01%; $k = 5.39\times10^{-2}$ min^{-1}; approximately pure $BaTiO_3$ × 7.8	Continuous core-shell interface provides a directional migration channel; oxygen vacancies improve light absorption and carrier dynamics	[35]
$BaTiO_3$/MoS_2 dual-piezoelectric heterojunction	Type-II chemically bonded heterojunction	Piezo-photocatalysis (NR)	Model catalytic reaction	BM-10 exhibits optimal performance; compositional ratio shows a volcano-type trend	Ti 3d orbitals and S 3p orbitals hybridize to form chemical bonds; Fermi level equilibration produces a built-in electric field	[52]
n-TiO_2/$BaTiO_3$/p-TiO_2 system, TBT3 sample	p-n dual heterojunction	Piezo-photoelectrocatalysis (stirring, 0-800 rpm)	Carrier dynamics	Carrier lifetime 1.88→3.28 ns; separation efficiency 43.6%→86.6%; further increasing the outer TiO_2 leads to performance decline	Inner and outer TiO_2 and $BaTiO_3$ form dual interfaces; the optimal ratio reduces transport resistance and mitigates agglomeration effects	[63]
S-scheme $BaTiO_3$/TiO_2 thin film	S-scheme heterojunction	Piezo-photocatalysis (40 kHz, 100 W)	Norfloxacin removal	60 min removal rate 91.7%; $k = 43\times10^{-3}$ min^{-1}; that of pristine TiO_2 × 2.69	Holes and ·OH are the primary reactive species; S-scheme pathway preserves strongly oxidizing holes	[67]
$AgNbO_3$/Pt@HA system	Schottky interface	Pure ultrasound (NR)	Tumor therapy	Tumor interstitial fluid pressure decreased by 48.16%; CAF apoptosis 59.4%; solid stress decreased by 44.07%; $CD8^+$ and $CD4^+$ T cells increased by 3.95-fold and 3.00-fold, respectively	Pt captures interfacial electrons and decomposes endogenous H_2O_2 to replenish O_2; $AgNbO_3$ piezocatalytically splits water to generate H_2 and ·OH	[70]
MoS_2/MXene atomic-thin-layer heterojunction	Schottky heterojunction; two-dimensional interface	Pure ultrasound (1.07 MHz, 0.309 W/cm^2, 10 s × 50 cycles)	Tumor therapy	Two-dimensional interface simultaneously provides short transport pathways, an electron sink, and nanozyme activity	Atomic-thin-layer interface shortens carrier migration distance; Schottky interface suppresses electron backflow	[69]

Note: Piezo-photocatalytic entries illustrate interfacial design principles; their rate constants are not transferable to ultrasound-only conditions *in vivo*.

To address the issues described in the first part of this section, two potential solutions can be considered. The first solution is to use two-dimensional van der Waals heterojunctions which have been found to remove dangling bonds and interfacial defects and therefore reduce transport distance down to the level of individual atoms. It is believed that through high throughput screening, $NbOI_2$ is the best candidate among the 2,940 monolayers with a large piezoresponse [74]. A second approach is to combine a semiconductor and a ferroelectric at an interface to create a permanent dipole across that interface. Creating a permanent dipole across the interface will produce a continuous electric field for charge separation. It is also believed that the remnant polarization of the ferroelectric phase can sustain charge separation between ultrasonic stress cycles, thereby reducing the reliance on continuous mechanical work [75].

These are novel approaches to charge carrier management in the spatial dimension. The next section will describe how temporal dimensions are managed with defect engineering.

4. Strategy II: defect engineering and temporal-dimension carrier trapping

4.1 Mechanisms of defect engineering

Defect engineering controls these phenomena through localized energy levels [25]. Defects such as oxygen vacancies, sulfur vacancies, cation vacancies, and aliovalent doping determine local coordination and introduce discrete energy levels in the bandgap [25,31]. Shallow traps are able to temporarily trap electrons and holes. The release of trapped charge can be induced by thermal perturbation and piezopotential reversal, while interfacial reactions continue to consume the released trapped charges [30,76]. The depth of a trap determines its effective survival time, which can extend from nanoseconds to microseconds and even milliseconds [77]. On the other hand, traps that are too deep tend to bind a charge permanently, forming nonradiative recombination centers [30,31]. A high concentration of defects increases free carrier screening of the piezopotential, which limits the motion of the domain walls. Hence, creating reversible trapping and release mechanisms is the primary goal of defect engineering.

Mechanisms described above mainly involve trapping and releasing of charge carriers, but defects also have a direct impact on lattice polarization and surface reactivity [16,25,78]. These three effects are a combined result of the type of defect, charge state, concentration, and distribution. Defects serve three functions in piezocatalysis [25]. First, defects alter the bandgap and the Fermi level as well as trap depth, leading to a control of the generation, trapping, release, and migration of charge carriers. Second, defects induce local strain, coordination changes, and symmetry breaking, which create defect dipoles and stabilize polar shifted phases, thereby changing the piezoelectric response. Lastly, defects create undercoordinated sites, increasing the adsorption of O_2, H_2O_2, and H_2O, as well as reducing the energy barriers for interfacial reactions.

A defect can change piezoelectric response, carrier dynamics, and surface reactions at the same time. Enhancements in the production of ROS are not enough to explain the performance improvements. Thus, the three functions must be explored independently.

4.2 Defect regulation of charge transport and interfacial reactions

Of the three functions, charge carrier management includes extending the lifetime of the system. Evidence was provided by O_v-BOS ultrathin nanosheets [45]. This consisted of the alternate stacking of $[Bi_2O_2]$ and $[SiO_3]$ layers. Oxygen vacancies form selective trapping regions in different layers. The ultrasonically induced electrons and holes are captured in separate layers, thereby suppressing bulk recombination. Total ROS generation was improved by about an order of magnitude with enhancement in the $^1O_2$ and $\cdot OH$ signals. Cation vacancies have a similar function in extending the lifetime [79]. Vanadium-vacancy-rich $BiVO_4$ nanosheets produced more ROS with ultrasonic stimulation [80]. Dual-vacancy HTiO ultrathin nanosheets had both oxygen and titanium vacancies [81]. The two types of vacancies reorganized the local Density of States and constructed complementary trapping states. Anion-cation pairing can further extend the trapping capacity.

When evaluating carrier lifetime extension, the position of defects in the bulk and on the surface determines whether charges can access the reactive interface [82]. Dual-defect regulation in C_3N_5 and g-C_3N_4 minimizes bulk defects to reduce deep-trap losses while maximizing surface defects to improve the availability of surface sites for both the adsorption and subsequent reaction [83,84]. Because of this, the charges, excited ultrasonically, can reach the material's surface and participate in the generation of ROS with greater efficiency [85]. In a similar fashion, $Bi_4Ti_3O_{12}$ nanosheets use surface oxygen vacancies to decrease bandgap and enhance surface ROS generation [86,87].

Reactive surfaces can change both the reaction pathway and the products of a reaction. BiO_{2-x} nanosheets having oxygen vacancies created products

to support the concept [88]. Ultrasound generates a piezopotential of approximately 0.25 V, causing the band to iteratively drop across the O_2/ $\cdot O_2^-$, $\cdot O_2^-$/H_2O_2 and H_2O_2/ $\cdot OH$ reduction potentials in a cascade. The role of vacancies on the selectivity of products was advanced by sulfur-vacancy-engineered $ZnIn_2S_4$ nanosheets [89,90]. Based on a vacancy structure optimization, a combination of ultrasound exposure and sonication resulted in the generation of $\cdot O_2^-$, $^1O_2$, $\cdot OH$ and H_2O_2. The production of multiple oxidation species resulted in a synergistic combination of activities (the downstream immune effects are discussed in Section 8).

Beyond the use of vacancies to control the charge transfer pathways, aliovalent doping can create and stabilize vacancies as a result of charge compensation [25,31]. An example of this is Gd-doped ZnO nanobullets, which are rich in oxygen defects that promote electron-hole separation under ultrasound [91]. Zhong et al. [92] showed that in the HfO_2 system, dopants affect vacancy formation. 20% Mn substitution was found to reduce the bandgap and enhance the presence of oxygen vacancies. Density Functional Theory (DFT) was used to examine pure HfO_2, Mn substituted HfO_2, and oxygen vacancy supplemented Mn substituted HfO_2, and concluded that the presence of oxygen vacancies leads to a reconstruction of the density of states and a reduction in reaction barrier. In both cases, the presence of the variable valence of Mn was shown to have both an enzyme-like effect and a glutathione depletion effect, inducing *in vitro* ferroptosis and PANoptosis, respectively.

Figure 3 illustrates various representations of the aforementioned three defect regulation strategies: stratified carrier trapping using interlayer oxygen vacancies (O_v-BOS [45]), aliovalent doping with the presence of oxygen vacancies (charge compensation) and stabilization (Mn-HfO_2 [92]), and a cascade of oxygen reduction coupled to multi-enzyme activities (BiO_{2-x} [88]).

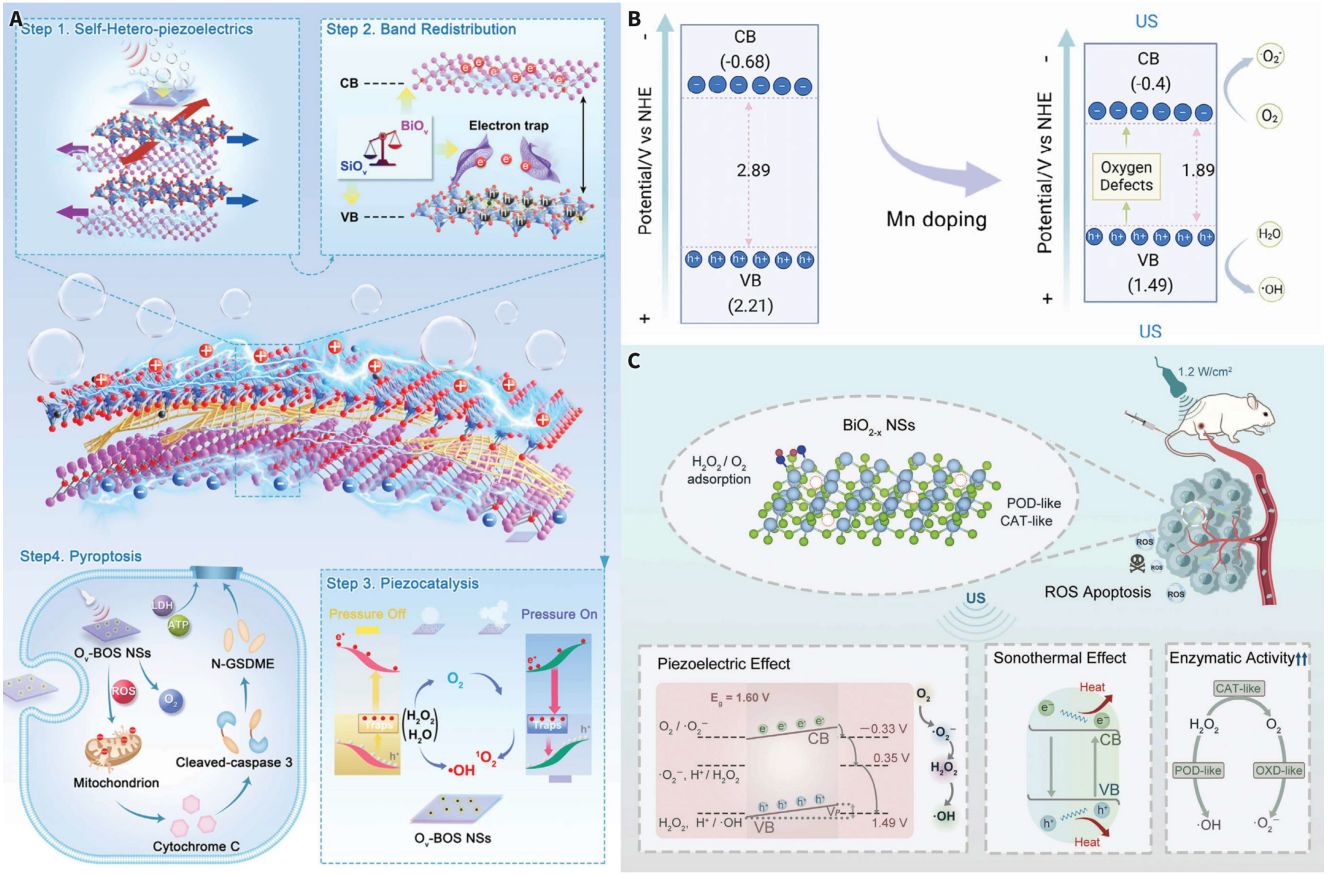


Figure 3. Defect engineering regulation of piezocatalytic carrier behavior and reaction pathways. (A) In O_v-BOS ultrathin nanosheets, alternately stacked [Bi_2O_2] layers and [SiO_3] layers form interlayer selective carrier trapping sites; electrons and holes are stored in separate layers to suppress bulk recombination, and upon ultrasonic activation, piezocatalytically generated ROS induce pyroptosis. Adapted with permission from Ref. [45]. Copyright 2025 Wiley-VCH GmbH. **(B)** Band structure engineering of Mn-doped HfO_2. 20% Mn substitution lowers the bandgap (2.89→1.89 eV) and introduces oxygen vacancy intermediate energy levels; the conduction band potential satisfies O_2 reduction and $\cdot OH$ generation, while valence band holes drive H_2O oxidation. Adapted with permission from Ref. [92]. Copyright 2025 the authors. **(C)** Oxygen-vacancy-rich BiO_{2-x} nanosheets exhibit a multimodal therapeutic mechanism under ultrasound. A piezoelectric potential of about 0.25 V shifts the conduction band across the O_2/ $\cdot O_2^-$, $\cdot O_2^-$/H_2O_2, and H_2O_2/ $\cdot OH$ reduction potentials in sequence, establishing a continuous oxygen-reduction cascade; oxygen vacancies simultaneously confer peroxidase-like and catalase-like activity on the material, and the coupling of piezocatalysis with these enzyme-like reactions amplifies ROS output. Adapted with permission from Ref. [88]. Copyright 2023 Wiley-VCH GmbH.

Table 2. Defect engineering evidence summary

Material System	Defect Type	Driving Condition	Evaluation Target	Key Performance Metrics	Defect Function Attribution	Reference
O_v-BOS ultrathin nanosheets	Interlayer oxygen vacancies	Ultrasound alone (1.0 MHz, 1.0–1.2 W/cm², 50% duty, 1–2 min)	Tumor therapy	ROS yield increased by about one order of magnitude; both $^1O_2$ and ·OH enhanced	Layer-selective carrier trapping suppresses bulk recombination	[45]
$BiVO_4$ nanosheets	Vanadium vacancies	Ultrasound alone (1 MHz, 1.2 W/cm², 50% duty, 5 min)	Tumor therapy	Increased available electrons; enhanced ROS	Cation vacancies extend carrier lifetime	[80]
HTiO ultrathin nanosheets	Oxygen vacancies + titanium vacancies	Ultrasound alone (1 MHz, 1.0–1.5 W/cm², 50% duty, 1–3 min)	Tumor therapy	Dual vacancies reconstruct the local density of states	Complementary trapping sites expand capture capacity	[81]
Dual-defect C_3N_5 / g-C_3N_4	Reduced bulk defects + increased surface defects	Ultrasound alone (NR)	Pollutant degradation / tumor therapy	Improved surface reaction efficiency	Fewer deep bulk traps + more surface active sites	[83,84]
$Bi_4Ti_3O_{12}$ nanosheets	Surface oxygen vacancies + corona polarization	Ultrasound alone (1 MHz, 1.0–1.5 W/cm², 50% duty, 5 min)	Tumor therapy	Narrowed bandgap; enhanced ROS	Surface oxygen vacancies suppress recombination	[86]
BiO_{2-x} nanosheets	Oxygen vacancies	Ultrasound alone (1.2 W/cm², 96 s)	Tumor therapy	Continuous oxygen-reduction cascade; piezocatalysis coupled with multi-enzyme-like activity	Oxygen vacancies enhance H_2O_2 adsorption; piezoelectric potential drives cascade reduction	[88]
$ZnIn_2S_4$ nanosheets	Sulfur vacancies	Ultrasound alone (1.0 MHz, 1.5 W/cm², 50% duty)	Tumor therapy	Simultaneous generation of $·O_2^-$, $^1O_2$, ·OH, and H_2O_2	Vacancy-modulated band edges + surface adsorption reshape ROS composition	[90]
Mn-doped HfO_2	Mn doping + oxygen vacancies	Ultrasound alone (1.0 MHz, 1.0 W/cm², 50% duty, 5 min)	Tumor therapy	Reduced bandgap; multi-enzyme-like activity; induces PANoptosis	Doping-induced charge compensation generates vacancies + variable-valence Mn confers enzyme-like activity	[92]
Bi_2WO_{6-x}	Gradient oxygen-vacancy concentration	Ultrasound alone (45 kHz, 60–100 W)	Hydrogen evolution	Volcano-type hydrogen-evolution rate; carrier concentration increases continuously while d_{33} progressively declines	Intermediate concentration balances carrier supply, piezoelectric polarization, and surface reaction	[97]

4.3 Defect function extension and concentration window

The extension of carrier lifetime, optimization of the defect distributions and re-engineering of the pathways of reaction are all functions that can be attributed to the inherent characteristics of the materials. There has been an ever growing body of evidence indicating that defects may provide additional functions that were not present in the material initially. For example, by creating Cu vacancy defects in the dielectric material $CaCu_3Ti_4O_{12}$, it is possible for the material to perform as a piezocatalyst [93]. In this scenario, the material generates H_2O_2 and ROS under combined ultrasound and light. For those materials which exhibit piezoelectric properties prior to the introduction of defects, defects can be introduced to regulate the spatial and temporal distributions of the catalytic output. CuFe based ultrathin nanozymes demonstrate decreased enzyme-like activity due to oxygen and metal vacancy defects; however, when subjected to ultrasound, the nanozyme-like activity returns to normal levels during the application of the ultrasound [94]. $BiFeO_3$ also exhibits the capacity to increase piezocatalytic activity via controlled oxygen vacancies [95]. Additionally, La-$BiFeO_3$ is capable of achieving spatial targeting [96]. La^{3+} ions released from the system disrupt the membranes of lysosomes with ROS, resulting in cell death.

The Bi_2WO_{6-x} piezocatalytic hydrogen-evolution system provides evidence of a typical volcano-type concentration relationship [97]. As the concentration of oxygen vacancies increases, the piezoelectric coefficient decreases, while the concentration of carriers continues to grow. At lower defect concentrations, the number of charge-trapping and surface-active sites are insufficient, thus limiting the rate of the interfacial reaction. At intermediate defect concentrations, there is a balance between piezoelectric polarization, surface reaction, and the number of carriers at the surface.

At elevated defect levels, deep-level traps create free-carrier screening and domain wall pinning. This results in a decrease of the piezoelectric effect and the loss of charge separation and its utilization. Bi_2WO_{6-x} is one of the very few systems in which an absolute defect concentration corresponds directly with performance. Further developments in the biomedical field will require an understanding of the parameters

within which one can work in terms of physiological media and therapeutic dose, both of which will be defined by quantitative assessment of defect concentration, therapeutic efficacy, and biosafety. The driving system, assessment objectives, and principal performance indicators for the systems outlined above are compiled in Table 2.

4.4 Construction and verification of defect structures

The construction of defects involves matching the depth and distribution of the target defects. For increasing both bulk and surface oxygen vacancies, either hydrogen or vacuum annealing methods can be used; however, these methods can lead to particle sintering, phase changes, and over-reduction, especially at high temperatures. Pd-catalyzed low-temperature hydrogenation can lower the temperature of the reaction and, at the same time, introduce defects and generate metallic electron sinks and enzyme-like sites (the Schottky contact mechanism of noble metals is described in Section 3.1). For shallow defects in ultrathin nanosheets, use of $NaBH_4$ and other chemical reduction methods are appropriate. These methods can be scaled easily to a large volume. However, leftover reducing agents and surface ligands can impair the biological interface of the system; as such, additional purification and surface composition assessment are warranted. Plasma treatments, ion bombardment, and photochemical etching remain focused on the surface of the material, and due to their lower thermal load, are suitable for creating surface and gradient vacancies [98,99]. When defects of greater stability are needed, doping is an appropriate method. Aliovalent doping stabilizes vacancies by charge compensation, but isovalent doping controls the vacancy formation energy by modifying the local strain. Doped systems also need to be assessed for ion leaching and long-term toxicity. The selection of a method should first evaluate if the defect is in the bulk, at the surface, or in the subsurface, and then determine the method based on strength of reduction, thermal load, the scale of application, and the anticipated condition of the system after treatment.

With the construction of the intended defect accomplished, the next step involves establishing if the constructed defect has changed the charge carrier transport. This subsequently determines if the constructed defect affects the reaction of the target species of ROS and the biological effects that are induced.

The first three questions to locate defects are site, concentration, and local valence state [25,30,31]. The peaks of high binding energy in O 1s XPS are often associated with hydroxyl and adsorbed oxygen. Therefore, oxygen vacancies are evaluated with other methods [25]. Electron paramagnetic resonance (EPR) is effective for the detection of paramagnetic defects and the assessment of the relative concentrations of spins [35]. The local coordination and valence state are accessible through atomically resolved scanning transmission electron microscopy with electron energy loss spectroscopy (STEM-EELS), X-ray absorption and Positron Annihilation Defect Spectroscopy. The local structural vacancies are evaluated using positron annihilation. Once confirmed structurally, the carriers' lifetime, along with their migration, is assessed using transient absorption, time-resolved PL or surface photovoltage techniques. These results are correlated with the respective defect concentrations [22,100]. Regarding ROS, attribution should be able to distinguish the type of species along with the origin of the oxygen atom. Endpoint fluorescence probes provide only a bulk measure of oxidizing species. Still, *in situ* EPR, when done under ultrasound, is able to detect specific radicals [35]. Isotope labeling with $H_2{}^{18}O$ or ${}^{18}O_2$ could further be used to trace the origin of the oxygen atom. These techniques should be done using treated samples with matching morphology, under the same ultrasound dose. This includes reduced samples, re-oxidized samples, and defect-free samples [35].

Once the structure-function correlation has been done, it must also be ascertained whether the intended state of the defects remains the same under cyclic ultrasound and in biological fluids.

Oxygen vacancies can be filled by dissolved oxygen and water, while ligands, protein corona, and phosphate groups can occupy surface active sites [25]. The changing stress resulting from cyclic ultrasound may also induce defect migration and localized reconstruction, and during the treatment, it may cause the energy levels and reactivity to change [101]. Metal-doped systems must also consider the leaching of ions and the associated health impact due to the burden on the liver and kidneys [31]. Surface or subsurface reversible traps along with degradable coatings can be used to limit the exposure time of active sites [102]. *In situ* liquid-phase electron paramagnetic resonance (EPR) can help observe defect progression, while valence-state analysis (before and after) of cyclic ultrasound can help identify structural changes, and long-term studies (*in vivo*) can investigate the tissue ion leaching and the pharmacokinetic distribution to study the clearance of leached ions [101]. Only the combination of these studies linked in one process can help determine if defect structure modulation is stable for an actual treatment cycle. The following section will examine how piezoelectric hydrogels link solid-state electrons, liquid-state ions, and the electrical

signals of tissues.

5. Strategy III: piezoelectric hydrogels with multi-dimensional catalyst-medium electrochemical coupling

5.1 Physical basis of mechanoelectrical transduction in the wet state

This section examines three separate types of hydrogel systems that can be distinguished based upon their principal mode of action. These types relate differently to the carrier-recombination model of this review: piezocatalytic hydrogels fall directly within it, electrical-stimulation hydrogels relate to it only indirectly, and piezoionic hydrogels lie outside it. Piezocatalytic hydrogels are able to generate piezoelectric charges as a result of mechanical stimulation. These generated charges then facilitate interfacial oxidation/reduction reactions leading to the generation of ROS and/or other reactive species. Piezoelectric electric-stimulation hydrogels create electrical signals or surface potential changes as a result of mechanical deformation. These generated signals/potentials influence cellular activity via bioelectrical signals, i.e., promoting proliferation of cells, differentiation of cells, and macrophage polarization. While ROS generation is a secondary effect in this category of hydrogels, the primary therapeutic effect is an electrical signal. Piezoionic hydrogels produce either streaming potentials or ionic currents as a result of mechanical deformation [103-105]. The production of either streaming potentials or ionic currents is a consequence of pressure-gradient-induced migration of ions through the polymer network. Unlike piezoelectric materials, the production of either streaming potentials or ionic currents is not due to crystallographic piezoelectricity.

The mechanisms incorporated in the previous two sections are concerned with the creation, transport, and recombination of solid-state charge carriers. The mechanisms share the common idea of long-distance carrier movement within the solid-state structure. A piezoelectric hydrogel adds a continuously hydrated environment, allowing charge carriers to be used in solid-state systems on three different levels [32,106-108].

The first of these levels is the ionic conductivity of the hydrogel. Hydrogel ionic conductivities can reach levels on the order of 1 S/m [33,109], which is already greater than that of solid-state oxide semiconductors. The polarization charge, which is created on the surface of the piezoelectric particles, is rapidly screened and compensated by the hydrated ions of the aqueous medium, and the formation of an interfacial electrical double layer undergoes formation, disruption, and reconstruction during each ultrasonic cycle. Thus, the piezoelectric field is enabled to participate directly in the electrochemical reduction of oxygen and the oxidation of water, so that the electrochemical process is no longer limited by the long-range electronic transport within the solid phase to the surface of the particles [32,107,110].

The second level is concerned with the mechanical properties of the gel matrix, which affects how efficiently the mechanical energy of the ultrasound is coupled to the piezoelectric particles.

Hydrogels usually have a modulus between 1 and 100 kPa [32,33]. This is comparable to or lower than the modulus of biological tissues. For example, the modulus of brain tissue is approximately 0.5 kPa, muscle is approximately 10 kPa, and cartilage is 1 MPa. If the modulus of the hydrogel is too low, the particles would behave as if they were suspended freely in a medium. If the modulus of the hydrogel is too high, tissue would behave as if the hydrogel and the tissue were in mechanical equilibrium. In between the two extremes, the hydrogel and the tissue would have interfacial stress concentrations. Thus, the hydrogel matrix would concurrently function as a biophysical match layer and as a mechanical transducer [32,111].

Next, the expanded and swollen network in highly hydrated hydrogels increases the effective zone in which many of the particles are contained. The majority of piezocatalytic processes are localized to the particle-liquid interface in a particulate matter suspension. When ROS are generated, they have to diffuse a considerable distance to the targeted cells. For piezoelectric particles in a hydrogel, the interparticle distance is on the micrometer scale. A closer distance would minimize the diffusion of ROS. The diffusion of ·OH is on the order of nanometers and the action radius of $^1O_2$ is within tens to hundreds of nanometers [112-114]. This means the spatial location of the particles is extremely important in order to achieve a therapeutic response.

5.2 Deployment strategies and representative studies

Piezoelectric hydrogel deployment formats can be divided into two categories, surface immobilization and injectable, and activation modes can be divided into ultrasound-driven and motion-driven.

In surface-immobilized systems, the hydrogel covers the wound or implant surface as a patch or coating. A 3D-printed Janus piezoelectric patch disperses $BaTiO_3$ nanoparticles within a hydrogel substrate; upon ultrasound activation, ROS are generated *in situ* at the patch-wound interface, achieving antibacterial activity and promoting wound

healing [115]. 3D-printed and conductive guar gum-based piezocatalytic hydrogels have demonstrated effective antibacterial activity in infected-wound models [116,117]. A piezocatalytic Pt@BMO gel dressing generates H_2 and NO *in situ* in an incontinence-associated infected-wound model, providing simultaneous antibacterial activity and suppression of neurogenic inflammation [37]. A gradient-porous piezocatalytic hydrogel foam achieves combined antibacterial activity and tissue repair in a pressure-ulcer infection model through the combination of *in situ* hydrogen generation and electrical stimulation [118].

Injectable piezoelectric hydrogels disperse piezoelectric particles within an in-situ-crosslinking gel precursor, forming a continuous piezoelectric network locally after injection into the joint cavity, tendon-bone interface, or tissue interstitium. The primary mechanism of action in the joint- and tissue-repair studies below is piezoelectric electrical stimulation and mechanical support, with only an indirect relationship to the carrier-recombination framework. PLLA nanofibers embedded in an injectable hydrogel were used for osteoarthritis treatment; low-intensity ultrasound activates the piezoelectric response, and cartilage regeneration and inflammation relief were observed in a rabbit knee model [111]. An injectable piezoelectric hydrogel accelerated repair in a tendon-bone healing model by remodeling the electrophysiological microenvironment and promoting M2 macrophage polarization [119]. A piezoelectric-conductive integrated hydrogel scaffold simultaneously provided piezoelectric stimulation and a conductive signal-transduction pathway in osteochondral defect repair [120], and an injectable self-healing $CaTiO_3$ hydrogel showed ultrasound-triggered antibacterial activity *in vitro* [121].

Motion-driven and ultrasound-driven activation constitute two complementary modes. Motion-driven activation has already been validated *in vivo* in rabbit knee cartilage regeneration: a PLLA piezoelectric scaffold generates sufficient electrical stimulation to promote cartilage repair under normal gait loading, providing relatively complete translational evidence encompassing mechanical testing, histology, and long-term follow-up, although the primary mechanism is piezoelectric electrical stimulation [122]. Ultrasound-driven activation is suited to scenarios such as wounds, deep tissues, and implant interfaces that cannot rely on motion loading. A low-intensity focused ultrasound-activated piezoelectric gel bandage achieved both wound repair and relief of diabetic neuropathic pain in a diabetic-wound model, although the original report notes that LIFU parameters require re-evaluation in large animals and humans [123]. In another diabetic-wound study, an ultrasound-responsive hydrogel remodeled immune regulation and neurovascular regeneration within the wound microenvironment through interfacial ion/electron transfer [124].

The deployment format, driving conditions, and key performance indicators of the systems described above are summarized in **Table 3.** Schematic illustrations of the mechanisms for four representative deployment strategies are shown in **Figure 4**: an injectable ultrasound-triggered piezocatalytic composite hydrogel for bacteria-infected wound healing [107], a dual-modal piezocatalytic-chemodynamic hydrogel for drug-resistant bacterial burn wounds [38], an interfacial ion/electron-transfer hydrogel for electrotherapy of diabetic wounds [124], and a biomimetic mechanoelectric ionic hydrogel for cartilage regeneration [125].

5.3 Design Principles

This body of work proposes four central pillars of piezoelectric hydrogel design.

The first pillar is the piezoelectric phase content. If this content is too low, the interparticle spacing is too large, resulting in a discontinuous effective reaction zone. However, if the content is too high, the gel network will lose continuity and mechanical integrity. From the literature, the piezoelectric phase content is generally 1 wt% or lower, as higher or lower contents affect ROS yield or electrical output and the mechanical properties of the gel [107,115,116]. High filler content also renders the gel optically opaque and increases acoustic scattering and impedance mismatch with tissue, which limits optical monitoring and attenuates ultrasound across thick gel layers.

The second pillar is that the gel modulus should correspond to the target tissue. Wound healing gels should have a modulus in the kPa range to closely match the modulus of the skin and subcutaneous tissue. Scaffolds for joint repair and support should have a higher modulus to support the repeated mechanical loading, and scaffolds for bone repair should consider the changing modulus of the scaffolds after mineralization. The success of the PLLA nanofiber/injectable hydrogel for osteoarthritis was due to the matching of gel modulus to articular cartilage [111]. The piezoelectric-conductive integrated scaffold used a dual network design to provide conductivity as well as mechanical strength [120].

The third pillar is the incorporation of conductive fillers. Adding conductive polymers, such as PEDOT:PSS, to a gel matrix, or carbon materials or MXene, improves charge transfer from the

piezoelectric phase to the liquid phase. The addition of a conductive component to a guar gum/PEDOT:PSS/BTO composite hydrogel, for example, enhanced piezocatalytic antibacterial activity [117]. Within the context of an insulating gel matrix, conductive fillers can also act as electron-conduction bridges, thereby reducing charge loss.

The fourth pillar is the adjustment of the degradation rate to the repair window. For implantable or injectable systems, gel degradation should align with tissue repair cycles. If degradation occurs too fast, premature particle release happens, causing loss of their local enrichment. If degradation occurs too slowly, it delays the growth and remodeling of new tissue. The PLLA-based system degrades to lactic acid, which has a large safety data repository. The rate of degradation can be adjusted with the changes in molecular weight and crystallinity. The injectable self-healing hydrogel can achieve controlled degradation with a dynamic crosslinking method. In the model of osteoarthritis, the degradation interval aligns with the cartilage repair cycle [111,121].

5.4 Tissue Response and Current Limitations

Piezoelectric hydrogels can respond to many biological models with a functional tissue response. For example, a PVA-based piezoelectric hydrogel accelerated wound closure and tissue remodeling in the form of a self-powered electrical stimulation system for diabetic wounds [126]. A chitosan-based bilayer structure had an electrical signal that was generated by the piezoelectric layer, and that electrical signal was then conducted through the hydrogel layer to the wound bed, thus creating a platform for neurovascular regeneration and a reduction in the amount of scar tissue formed [127]. A periodontitis model showed that a piezoelectric hydrogel increased the rate at which periodontal tissue repaired itself through bioenergetic activation [128]. There are preliminary reports on how piezoelectric ionic hydrogels affect the movement of tumor cells. A mechano-bioelectric ionic hydrogel (which is similar to endogenous ionic electrical signaling) had both the cartilage regeneration effect as well as the piezoionic response of native articular cartilage [125].

Table 3. Piezoelectric hydrogel evidence summary

Material System	Deployment Format	Driving Condition	Evaluation Target	Key Performance Indicator	Primary Mechanism of Action	Reference
$BaTiO_3$/Janus patch	Surface immobilization	Ultrasound (1.0 MHz, 1.5 W/cm², 50% duty, 3 min)	Infected wound	*In situ* ROS generation; antibacterial + healing	Piezocatalysis	[115]
3D-printed BTO/hydrogel; cast guar gum/PEDOT:PSS/BTO hydrogel	Surface immobilization	Ultrasound (0.5–1.5 W/cm², 5 min)	Infected wound	Antibacterial effect	Piezocatalysis	[116,117]
Pt@BMO gel dressing	Surface immobilization	Ultrasound (0.5–1.5 W/cm², 30 min)	Incontinence-associated infected wound	*In situ* H_2 and NO generation; antibacterial + anti-inflammatory	Piezocatalysis	[37]
Gradient-porous hydrogel foam	Surface immobilization	Ultrasound (NR)	Pressure ulcer	*In situ* hydrogen generation + electrical stimulation; antibacterial + repair	Piezocatalysis + electrical stimulation	[118]
PLLA nanofiber/injectable hydrogel	Injectable	Ultrasound (40 kHz, 0.33 W/cm², 20 min)	Osteoarthritis	Rabbit knee cartilage regeneration; inflammation relief	Piezoelectric electrical stimulation	[111]
Injectable piezoelectric hydrogel	Injectable	Mechanical loading	Tendon-bone healing	M2 macrophage polarization; accelerated repair	Piezoelectric electrical stimulation	[119]
Piezoelectric-conductive integrated scaffold	Implantation	Motion (joint loading)	Osteochondral defect	Dual piezoelectric + conductive signal pathway	Piezoelectric electrical stimulation	[120]
PLLA piezoelectric scaffold	Implantation	Motion (gait)	Cartilage regeneration	Mechanical testing + histology + long-term follow-up	Piezoelectric electrical stimulation	[122]
Piezoelectric gel bandage	Surface immobilization	LIFU (1.0 MHz, 1.5 W/cm², 50% duty, 120 s)	Diabetic wound	Wound repair + relief of neuropathic pain	Piezoelectric electrical stimulation	[123]
Ultrasound-responsive hydrogel	Surface immobilization	Ultrasound (1 MHz, 0.5–2.5 W/cm², 20–50% duty)	Diabetic wound	Immune modulation + neurovascular regeneration	Interfacial ion/electron transfer	[124]
PVA-based piezoelectric hydrogel	Surface immobilization	Self-powered	Diabetic wound	Wound closure + tissue remodeling	Piezoelectric electrical stimulation	[126]
Chitosan-based bilayer hydrogel	Surface immobilization	Ultrasound (1 MHz, 1.2 W/cm²)	Diabetic wound	Neurovascular regeneration + scar reduction	Piezoelectric electrical stimulation	[127]
Piezoelectric hydrogel	Injectable	Ultrasound (1 MHz, 0.6 W/cm², 50% duty, 60 s)	Periodontitis	Periodontal tissue repair	Piezoelectric electrical stimulation	[128]
3D-bioprinted piezoelectric hydrogel	Implantation	LIPUS (0.2 W, 20% duty, 5 min)	Bone regeneration	Synergistic effect of piezoelectricity and low-intensity pulsed ultrasound (LIPUS)	Piezoelectric electrical stimulation	[129]
Piezocatalytic scaffold	Implantation	Ultrasound (100 kHz, 0.7 W/cm², 20 min)	Diabetic bone regeneration	Antioxidant cycling; bone repair	Piezocatalysis	[130]

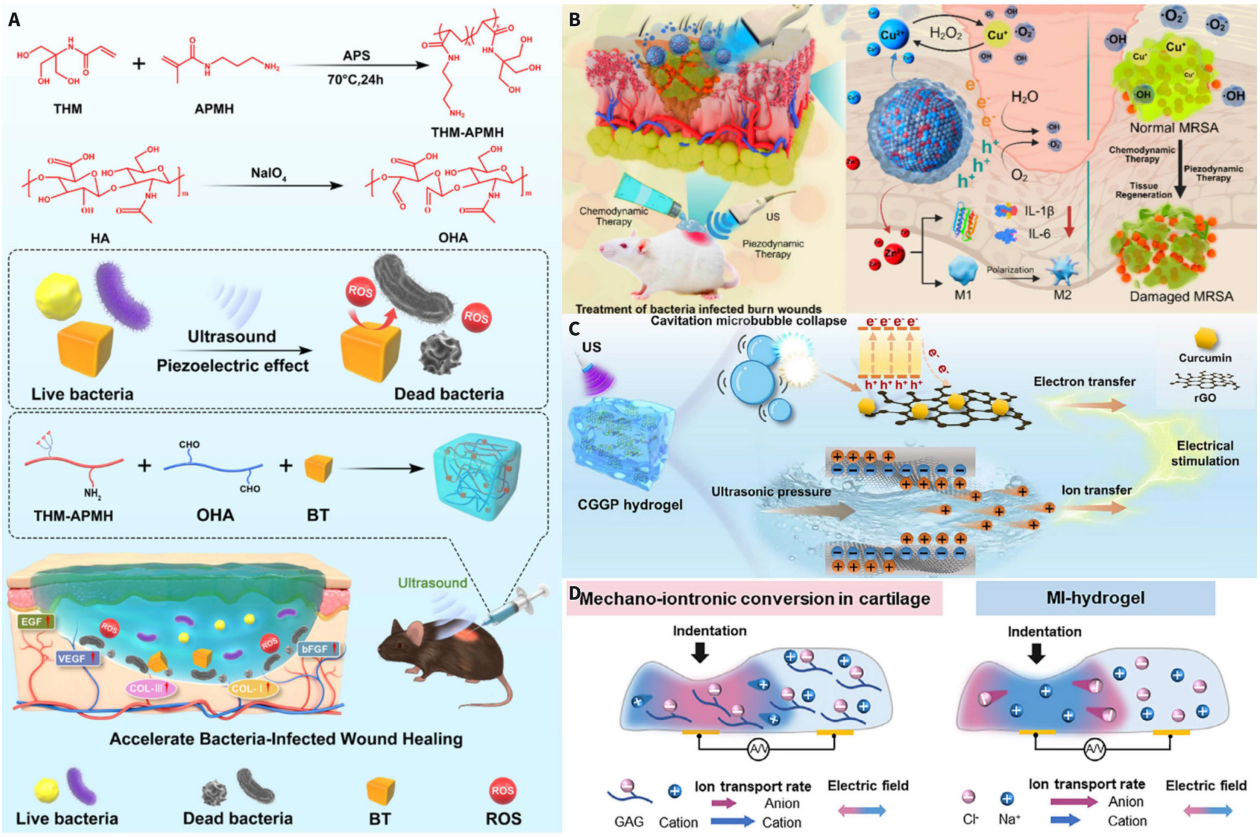


Figure 4. Representative deployment strategies for piezoelectric hydrogels across different biomedical scenarios. (A) Injectable BT-OHA/THM-APMH piezocatalytic composite hydrogel generates ROS under ultrasound for antibacterial treatment and accelerated healing of bacteria-infected wounds. Adapted with permission from Ref. [107]. Copyright 2022 the authors. **(B)** Cu_5Zn_5@BTO hydrogel achieves synergistic piezocatalytic and chemodynamic dual-pathway therapy for MRSA-infected burn wounds. Adapted with permission from Ref. [38]. Copyright 2025 Elsevier Ltd. **(C)** CGGP ultrasound-responsive hydrogel enables electrotherapy for diabetic wounds through interfacial ion/electron transfer. Adapted with permission from Ref. [124]. Copyright 2025 Wiley-VCH GmbH. **(D)** A biomimetic mechano-bioelectric ionic hydrogel mimics the piezoionic response of native cartilage GAGs, generating endogenous bioelectric signals to promote cartilage regeneration. Adapted with permission from Ref. [125]. Copyright 2025 Wiley-VCH GmbH.

There remains a disconnect in the ability to advance functional systems and delineate their mechanisms.

This is a previously unstudied area of research regarding how to measure the charge or potential changes occurring in-situ as a result of the force applied to the piezoelectric particles and the subsequent formation of the interface layer. There has been little if any research on the effect of the solid phase piezoelectric polarization or streaming potential on the system. All but one of the studies have used the same ultrasound conditions for bare-particle systems, without accounting for the differences in acoustic impedance and stress-transfer characteristics of particles embedded in a polymer hydrogel matrix. Composite hydrogel systems deform very differently than empty matrices. Another major challenge will be distinguishing between the actual piezocatalytic effect and non-piezoelectric effects associated with ultrasound exposure such as thermal effects, radiation forces and acoustic streaming. It is particularly important to distinguish these from piezocatalytic effects in polymer-matrix systems since they absorb significant amounts of heat. In order to determine the specific contributions of piezocatalysis, future studies must incorporate matched non-piezoelectric controls, such as a centrosymmetric isomorph, a sample depolarized above its Curie temperature, or non-piezoelectric particles of comparable size and surface chemistry. To date, almost none of the published studies have incorporated such controls, thereby limiting their capacity to attribute the observed effects to the piezocatalytic mechanism.

It is possible to combine the three strategies in multiple ways; the next step is to determine how to optimally choose and combine them for the application of interest.

6. Strategy selection and combination rules

6.1 Strategy selection derived from the target application

Prior to introducing the decision tree, it is beneficial to summarize the advantages and disadvantages associated with each of the three

primary approaches. Heterojunction engineering (spatial aspect) has been shown to produce significantly greater improvements in carrier separation efficiency, such as those produced with the $BaTiO_3@TiO_{2-x}$ system which exhibited a 7.8 times increase in reaction rate relative to its own unmodified control under combined light and ultrasound. However, heterojunction engineering performance is dependent upon the quality of interfacial bonds formed, and there is a high degree of variation in performance from batch-to-batch. In addition, the built-in electric fields generated through heterojunction engineering can be diminished due to screening effects caused by mobile ions found in high-ionic strength physiological fluid environments. Defect engineering (temporal aspect) is a relatively simple single-phase technique that can significantly improve the rate of catalysis, sometimes increasing it by as much as an order of magnitude relative to its own control (O_v-BOS). The downside to defect engineering is that there is only a small range of defect concentrations that will provide optimal catalytic activity. Too many defects can permanently decrease the catalytic activity of the material. Finally, piezoelectric hydrogels (catalytic medium aspect) combine the catalyst, the aqueous solution where the reaction takes place, and the biological target into one location, thereby decreasing the distance required for ROS to diffuse to reach the biological target. However, the ability of the hydrogel to transmit mechanical energy to generate electric charges is limited, as is the rapid screening of electrical charges generated via mechanical stimulation by mobile ions present in the aqueous environment. A decision tree based on these trade-offs is presented below to allow researchers to determine which approach should be utilized first depending on the specific application.

The three nodes are: the therapeutic intent (catalytic killing or tissue regeneration), whether the lesion depth exceeds 5 cm, and whether the material will require implantation for a prolonged period of time.

The optimal treatment strategy for achieving a high ROS yield and addressing lesions that exist deep in a tissue is through a combination of using defect-engineered oxides along with low-frequency ultrasound. While 1.0–3.0 MHz piezocatalysis frequencies are typically used for shallow lesions, 0.5–1.0 MHz frequencies are preferred when treating lesions that are deeper in a tissue due to the fact that lower frequencies experience less tissue attenuation and can create enough acoustic pressure to reach target areas beyond 5 cm in depth. To limit the risk of inertial cavitation and tissue damage, the mechanical index (MI) should remain below the FDA diagnostic ceiling of 1.9. To limit the amount of heat generated during the process of creating acoustic pressure, the spatial-peak temporal-average intensity (I_{spta}) should not exceed the diagnostic limit of 720 mW/cm^2, although many therapeutic studies operate above this level and require separate safety assessment. Finally, to provide periodic mechanical stress on the lesion while limiting thermal deposition in the intervening tissues, a pulsed mode with a duty cycle of 10–50% should be employed. By utilizing these parameters, we can achieve adequate acoustic penetration and generate sufficient piezopotential to treat the lesion, while remaining below the thresholds for both cavitation-induced tissue damage and thermal-induced tissue damage. It is possible to increase the catalytic activity of a single particle through the use of defect engineering, without needing to construct an interface between different materials. This approach can be applied as long as the concentration of defects falls within the ascending portion of a volcano-shaped curve, and the majority of defects are located at or close to the surface of the material [25,97]. However, if there are too many defects present, they may act to block the polarization field, or if they occur deeply in the material, they may function as recombination centers. Therefore, it is necessary to determine the optimal defect concentration experimentally for each individual application [25,97]. If the material system meets the criteria required for constructing a two-phase interface (band alignment, interfacial continuity), then we can use heterojunction engineering to further improve the performance of our device. For example, the $BaTiO_3@TiO_{2-x}$ core-shell system offers both a heterojunction interface and oxygen vacancies, therefore providing a better outcome than either approach would provide alone under combined light and ultrasound [35].

In the event that a high ROS yield application has a superficial lesion and prolonged implantation is not required, the recommended approach is the combination of a piezoelectric hydrogel and nanozyme. The hydrogel provides co-location of the material, reaction interface, and the biological target, thereby shortening the distance to which the ROS have to diffuse to reach the target cell before action is taken.

The relevant condition here is whether the lesion can be patched or filled by injection, where mechanical stimulation is maintained by ultrasound [32,115]. The failure condition is whether the gel matrix has too low a force-transmission efficiency or whether the aqueous environment has a severe polarization screening. To a limited extent, these can be compensated for by using conductive fillers and nanozymes [37,117].

Where the main action is tissue regeneration with the controlled action of ROS, then stimulation by

piezoelectric means becomes the main action. In the case of soft tissue repair, a piezoelectric hydrogel or a degradable PLLA scaffold, driven by motion or ultrasound, provides a controlled way of stimulating electrical activity to enhance the proliferation and differentiation of cells and the polarization of macrophages [111,122]. The main design constraints on this pathway will be to match the stiffness to the target tissue and to optimize the rate of scaffolding control to the repair process.

Implant-associated infection stays within the catalytic-killing branch because eradicating an established biofilm requires cytotoxic ROS, and what sets it apart from an infected wound is that the reactive surface must remain in place [131]. When the application target is implant-surface anti-infection and the material must stay permanently, a material platform with expressed clinical safety data may be prioritized. HfO_2 nanoparticles (NBTXR3) have received CE marking as a radioenhancer and are in phase III clinical trials. Pristine monoclinic HfO_2 shows only a modest piezoresponse, whereas Mn doping can enhance piezocatalytic activity, and atomic layer deposition can create a uniform film on the surface of the implant [92]. The existing HfO_2 toxicological data can serve as a reference baseline, although the doped formulation still requires independent safety evaluation (Section 9.1). Deep-seated implants follow the deep branch of the tree, where the same coating is driven with 0.5–1.0 MHz ultrasound, and the pathogen burden sets the ultrasound dose within this pathway.

The decision nodes, recommended strategies, and key design parameters for the four pathways mentioned above are in Figure 5 and Table 4. It should be noted that effective transport distance and effective carrier lifetime cannot yet be measured directly when ultrasound is in operation, the pathway selection for the above relies on the direction of endpoint performance to strategic changes, rather than on the absolute values of these two variables.

6.2 Multi-strategy combination and criteria for synergy

Synergy effects have been evaluated in numerous studies utilizing multiple strategy combinations. For us to differentiate a purely additive effect from a true synergistic effect, at least four separate control experiments must be performed under the same experimental conditions; namely, the unmodified sample, two separate singly modified samples and a single doubly modified sample. Only a few systems designed in this field have reported the use of all four control groups [59], including the iodine-doped $Bi_4Ti_3O_{12}$/MXene system. This system has reported the production rates of H_2O_2 for each of the four groups, thereby providing the necessary data to evaluate potential interactions. Most combined systems typically make comparisons between the best performing sample and the original unmodified sample. Therefore, most of the time there will be no singly modified control groups present, making it impossible to identify which modification contributed to the improved performance.

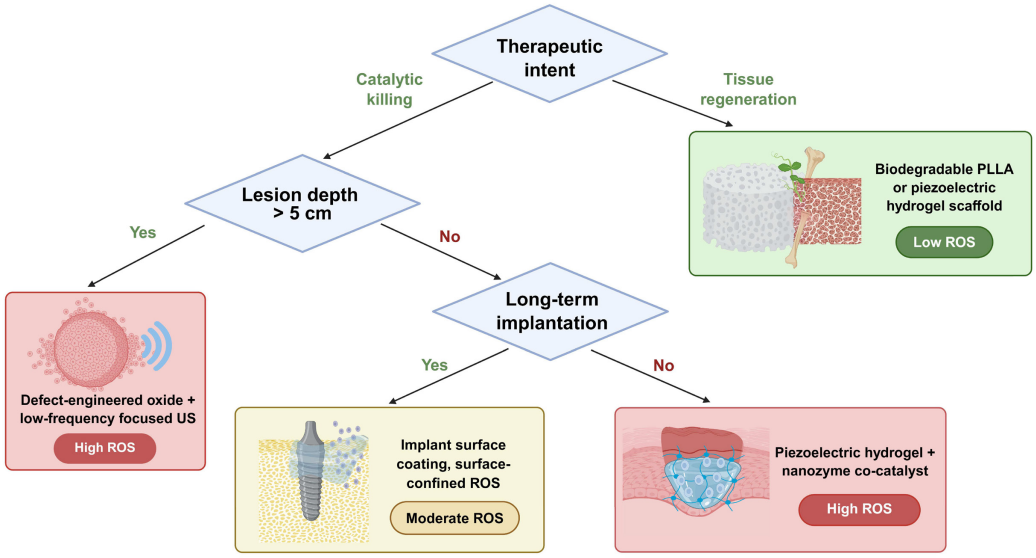


Figure 5. Clinical-parameter-based decision tree for piezocatalytic material design. Starting from the target application, the tree proceeds through three decision nodes in sequence: the therapeutic intent (catalytic killing vs. tissue regeneration), whether the lesion depth exceeds 5 cm (deep vs superficial), and whether the material requires long-term implantation (within the superficial catalytic-killing branch). The four terminal pathways correspond, respectively, to: defect-engineered oxide combined with low-frequency ultrasound (deep tumor), piezoelectric hydrogel combined with nanozyme synergy (infected wound), degradable PLLA scaffold or piezoelectric hydrogel (tissue regeneration), and Mn-doped HfO_2 thin film deposited onto the implant surface by atomic layer deposition (implant anti-infection). Each terminal is labeled with its ROS tier (high, moderate, or low). Created in BioRender. T. (2026) https://BioRender.com/b9yf96l. The recommended strategy, key design parameters, and pitfalls to avoid for each pathway are detailed in **Table 4.**

Table 4. Strategy selection decision framework

Application scenario	ROS demand	Lesion depth	Implantation	Recommended strategy	Key design parameters	Pitfalls to avoid
Deep tumor	High	> 5 cm	No	Defect-engineered oxide + low-frequency ultrasound; heterojunction engineering can be layered on	Defect concentration window; band alignment	Excess defects cause screening; deep traps cause recombination
Superficial infected wound	High	< 5 cm	No	Piezoelectric hydrogel + nanozyme synergy	Piezoelectric phase content ≤ 1 wt%; modulus matching	Insufficient force-transmission efficiency; polarization screening
Joint/bone/soft tissue regeneration	Low	Variable	Yes (biodegradable)	Piezoelectric hydrogel or PLLA scaffold	Modulus matching; degradation rate synchronization	Excessively fast degradation causes loss of local enrichment
Implant surface anti-infection	Moderate (surface-confined)	Surface	Yes (long-term)	Mn-doped HfO_2 thin film (ALD) + defect engineering	Film thickness uniformity; ion leaching control	Long-term leaching toxicity of dopant ions

The combination of heterojunction and defect engineering is the most prevalent, and also the most confused with regard to attribution. The $BaTiO_3$@TiO_{2-x} core-shell system has both a heterojunction interface and oxygen vacancies. The performance improvement has been attributed to this three-way synergy; however, the combined contributions of the heterojunction and the oxygen vacancies have not been separated. To assert that two strategies are indeed synergistic, at least four control groups should be documented with the key performance indicator stated for each.

The effect of the double modification may be considered synergistic if its performance exceeds that of the combined performance of each single modification. On the other hand, if the double modification does not perform better than the combined performance of each single modification, then the effect may be considered competitive (for example, defects blocking the heterojunction's electric field). In addition to being dependent upon the selection of the endpoint metric, there are several models available for assessing synergy depending on what type of endpoint was used. For example, for fractional cell survival data, the Bliss Independence Model would provide a suitable null hypothesis. For concentration-effect curves in which the agents share a common mode of action, Loewe Additivity would be most appropriate. Catalytic endpoints such as dye degradation rates or H_2O_2 yields can be analyzed using a simple rate-constant additivity model. Regardless of which model is used, it should be clearly indicated in the report so that comparisons can be made across studies.

Disentangling material-level strategies with hydrogel deployment integration across scales is even more challenging. In systems with both a modified piezoelectric particle and a hydrogel matrix, the deployment-level gain and the material-level gain can be separated only if a non-piezoelectric gel of the same composition is used as a control, a control that Section 5.4 has also stated is almost non-existent in the literature. In the absence of systematic multilevel arm control experiments, the combination of strategies should be limited by the failure conditions of each single strategy. The expected benefit of layering a second strategy is greatest when the critical parameter of the first strategy is already near its failure condition (e.g., when defect concentration is near the peak of the volcano-type curve, or when the shell thickness is near the minimum for continuous coverage).

7. Two-dimensional piezoelectric materials

2D piezoelectric materials have three structural benefits [40,74,132-135]. First, atomic-scale thickness reduces the distance that carriers must travel to cover the entire cross-section of the material and significantly reduces the probability of carriers recombining in the bulk of the material.

Next, a higher specific surface area means that nearly every atom is exposed at the reaction interface, creating a surface active-site density that is considerably greater than that of bulk materials. Additionally, the piezoelectric response is tunable based on the number of layers, stacking order, strain, and presence of defects. The crystal structures of selected three categories of 2D piezoelectric materials are depicted in Figure 6.

These materials include transition metal dichalcogenides [137], group-IV monochalcogenides [138], and oxygen-containing layered compounds. The in-plane piezoelectric coefficient of monolayer MoS_2 has been measured as shown in literature [136,139]. Janus MoSSe displays out-of-plane piezoelectric polarization because of the uneven arrangement of surface atoms, which breaks the out-of-plane mirror symmetry [40]. A recent high-throughput first-principles screening of 2940 monolayer materials found piezoelectricity in $NbOI_2$, predicting a coefficient that exceeds most 2D materials [74]. SnSe nanosheets utilize defect synergy to deliver a dual piezocatalytic and chemocatalytic antitumor effect under ultrasound [140]. Mitochondria-targeting 2D WS_2 nanosheets deliver piezocatalytic therapy with

energy metabolism intervention during ultrasound [141]. Enhancing dual-vacancy-engineered 2D sonocatalytic materials, which contain both anionic and cationic vacancies, sustains ultrasound-triggered PANoptosis [81]. 2D Bi_4NbO_8Br single-crystal nanosheets and 2D Bi_2MoO_6 nanobelts display significant ROS production and tumor suppression under the influence of ultrasound [142,143]. An atomically thin MoS_2/MXene Schottky heterojunction combines the short transport pathways of 2D materials with a metallic electron sink and provides both piezocatalysis and nanozyme in ultrasound-triggered tumor therapy [69]. Research has shown that modifying vacancies in 1T'-ReS_2 (which is normally non-piezoelectric) can render it piezoelectric, which can then be used for tumor therapy via ferroptosis using ultrasound [144].

Three key challenges face 2D piezocatalysis. First, large-scale controllable synthesis is complicated due to the fact that the multilayer nanosheets resulting from either chemical exfoliation or liquid phase synthesis are largely uncharacterized with respect to the layer-number distribution and stacking order, complicating quantitative responses to the measured piezoelectric response [40,74]. Second, the materials' atomic scale thickness undermines the long-term *in vivo* stability, as they are more prone to oxidation and degradation [40]. Lastly, in order to shorten the transport distance, defect density alterations are often required, but within the same manufacturing process, the two variables are inextricably linked, making it nearly impossible to separate the contributions to performance improvement [81,90,141]. This separation would require varying thickness with a constant defect density or a varying defect density with a constant thickness; as of now, only a few systems partially accomplish this [90].

8. Piezoelectric immunoengineering

Piezoelectric immunoengineering extends the therapeutic target of piezocatalysis from direct ROS-mediated tumor cell killing to modulation of the tumor immune microenvironment [145-147]. The underlying logic is as follows: piezocatalysis-generated ROS induce immunogenic cell death (ICD), releasing tumor antigens and damage-associated molecular patterns (DAMPs) that activate antitumor immune responses and thereby convert a localized treatment into a systemic immune effect.

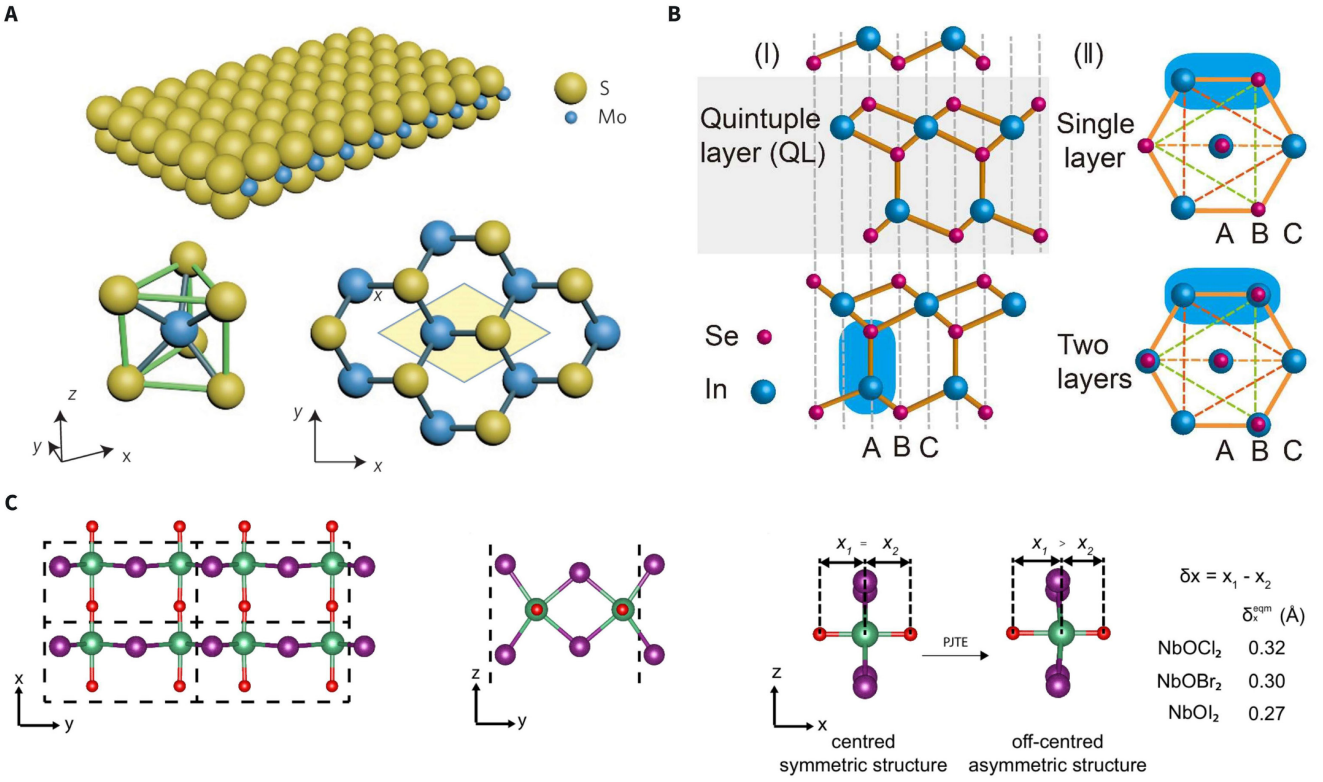


Figure 6. Crystal structures of representative 2D piezoelectric materials. (A) Single-layer MoS_2 with D_{3h} symmetry: the S-Mo-S stacking viewed in 3D perspective, the trigonal prismatic coordination unit, and the top view showing the hexagonal lattice with a rhombic unit cell (yellow shading). Adapted with permission from Ref. [136]. Copyright 2015 Macmillan Publishers Limited. **(B)** Non-centrosymmetric quintuple-layer (QL) α-In_2Se_3: (I) side view highlighting the Se-In-Se-In-Se stacking sequence, and (II) top view of single-layer and two-layer configurations. Adapted with permission from Ref. [135]. Copyright 2018 American Chemical Society. **(C)** Layered $NbOI_2$: top view, side view, and pseudo-Jahn-Teller effect (PJTE)-induced off-centering distortion converting a centred symmetric structure into an asymmetric one, with equilibrium displacement δx values for the $NbOX_2$ family. Adapted with permission from Ref. [74]. Copyright 2022 the authors.

The mechanistic link between material modification and immune activation is through specific ROS. The formation of sulfur vacancies in $ZnIn_2S_4$ nanosheets expands the conduction band to encompass the redox potentials of $O_2/\bullet O_2^-$, $H_2O_2/\bullet OH$ and $O_2/{}^1O_2$ concurrently. As a result, there is a production of multiple types of ROS ($\bullet O_2^-$, $^1O_2$, $\bullet OH$ and H_2O_2) that initiate immunogenic cell death (ICD) characteristics such as calreticulin exposure on the surface of dying cells and release of HMGB1; once released, damage-associated molecular patterns (DAMPs) promote dendritic cell maturation ($CD80^+CD86^+$) and infiltration of $CD8^+$ T cells into the tumor [90]. Oxygen-vacancy engineering in $CaBi_2Nb_2O_9$ activates phosphorylated RIPK3 and MLKL, initiating the necroptosis signaling cascade, and the DAMPs produced by necroptosis feed into the same dendritic cell maturation pathway as above [148]. Both cases demonstrate how the nature and quantity of ROS generated during material modification, regulated via defect-engineering, dictate which cell-death pathway will be induced, and how the resulting DAMPs propagate along the immune signaling hierarchy from molecular activation, through cellular responses to possible systemic effects.

Membrane-coated $BaTiO_3$ nanoparticles increase $CD8^+$ T cell infiltration through piezocatalysis combined with PD-L1 blockade [149], and ultrasound-driven piezoelectric stimulation promotes M1 polarization of macrophages via the Ca^{2+}-CaMKII-NF-κB axis [150]. The use of ultrasound-activated piezoelectric nanoparticles results in the ion-channel reprogramming of immune cells, leading to the rescue of immunosuppressed animals in lethal bacterial infection models [150,151]. Copper-vacancy Bi_2CuO_4 (BCO-V_{Cu}) synergistically combines piezocatalysis with Fenton-like reaction and GSH depletion, while its copper vacancies increase d_{33} [152]. In the context of innate immune sensing, activation of the cGAS-STING pathway by piezocatalysis has been reported in a liquid metal nanoparticle system [153]. In the context of immunogenic cell death, enhancement of pancreatic cancer immunotherapy by the release of NO via piezocatalysis [154], targeted catalytic immunotherapy of colorectal cancer with piezoelectric oral microrobots [155], and the remodeling of the tumor immune microenvironment by the inhibition of N-glycosylation and piezocatalysis [156] have also been reported. There is an intersection of immunoengineering and defect engineering in the use of defect-modulated ferroptosis and necroptosis to provide a basis for antitumor immunity [148,157,158] and the use of sulfur-vacancy-optimized $ZnIn_2S_4$ to activate immune responses via multi-species ROS output [90]. Piezoelectric nanomaterials can activate antitumor immune responses through multiple signaling pathways, including Ca^{2+}–NF-κB, necroptosis–DAMPs positive feedback, piezo-enhanced Fenton–ICD, and pyroptosis–cGAS-STING **(Figure 7A)**. The existing experimental evidence can be classified into three tiers based on the biological hierarchy of action, in decreasing order of strength.

At the molecular level, defect-engineered $CaBi_2Nb_2O_9$ under ultrasound upregulates p-RIPK3 and p-MLKL, directly confirming the activation of the necroptosis pathway **(Figure 7B)** [148]. At the cellular level, piezocatalysis induces immunogenic cell death (ICD) hallmarks, including calreticulin (CRT) exposure, HMGB1 release, and HSP70 expression **(Figure 7C)** [156], piezoelectric stimulation upregulates the transcription of TNF-α and IL-1β in macrophages **(Figure 7D)** [150], and piezocatalysis promotes dendritic cell (DC) maturation as well as $CD8^+$ T cell infiltration **(Figure 7F,G)** [90,149]. At the systemic level, the growth of distant untreated tumors in bilateral tumor models is inhibited **(Figure 7E)** [152], accompanied by increased intratumoral $CD8^+$ T cell infiltration **(Figure 7H)** [154] and a reduced number of lung metastatic nodules **(Figure 7I)** [159].

The causal chains at the molecular and cellular level of the three layers of evidence described above are fairly well established; however, systemic effects of piezocatalysis are typically achieved when combined with other forms of immunotherapy such as anti-PD-L1, anti-CTLA-4, or adoptive cell transfer. Therefore, it is difficult to determine what part of the piezocatalytic effect is independent. There is an important difference here: we have some level of certainty that the ICD induction and DAMP release that occur at the cellular level are due to piezocatalysis because these events are evaluated either *in vitro* or in individual tumor models in which no other type of immunotherapy was administered. On the other hand, the abscopal effects demonstrated in bilateral tumor models are typically produced by combination regimens, and it has yet to be determined whether it is the piezocatalysis-produced ROS or the co-administered immunotherapeutic agent that is responsible for producing the abscopal effect. While both traditional sonodynamic immunotherapy (which uses ultrasound-activated sonosensitizers to induce ICD) and piezoelectric immunoengineering produce ICD, there are two major ways that piezoelectric immunoengineering differs from traditional sonodynamic immunotherapy in terms of mechanism: first, the ROS generated during piezoelectric immunoengineering can be modified based upon the materials used (e.g., defects in the material, vacancy concentrations in the material, design of

heterojunctions within the material) [160], whereas in traditional sonodynamic immunotherapy the ROS composition is governed mainly by cavitation conditions and the sensitizer; second, the piezopotential created during piezoelectric immunoengineering can affect ion channel activity in immune cells (e.g., TRP-Ca^{2+} signaling) independently of any ROS-induced ICD.

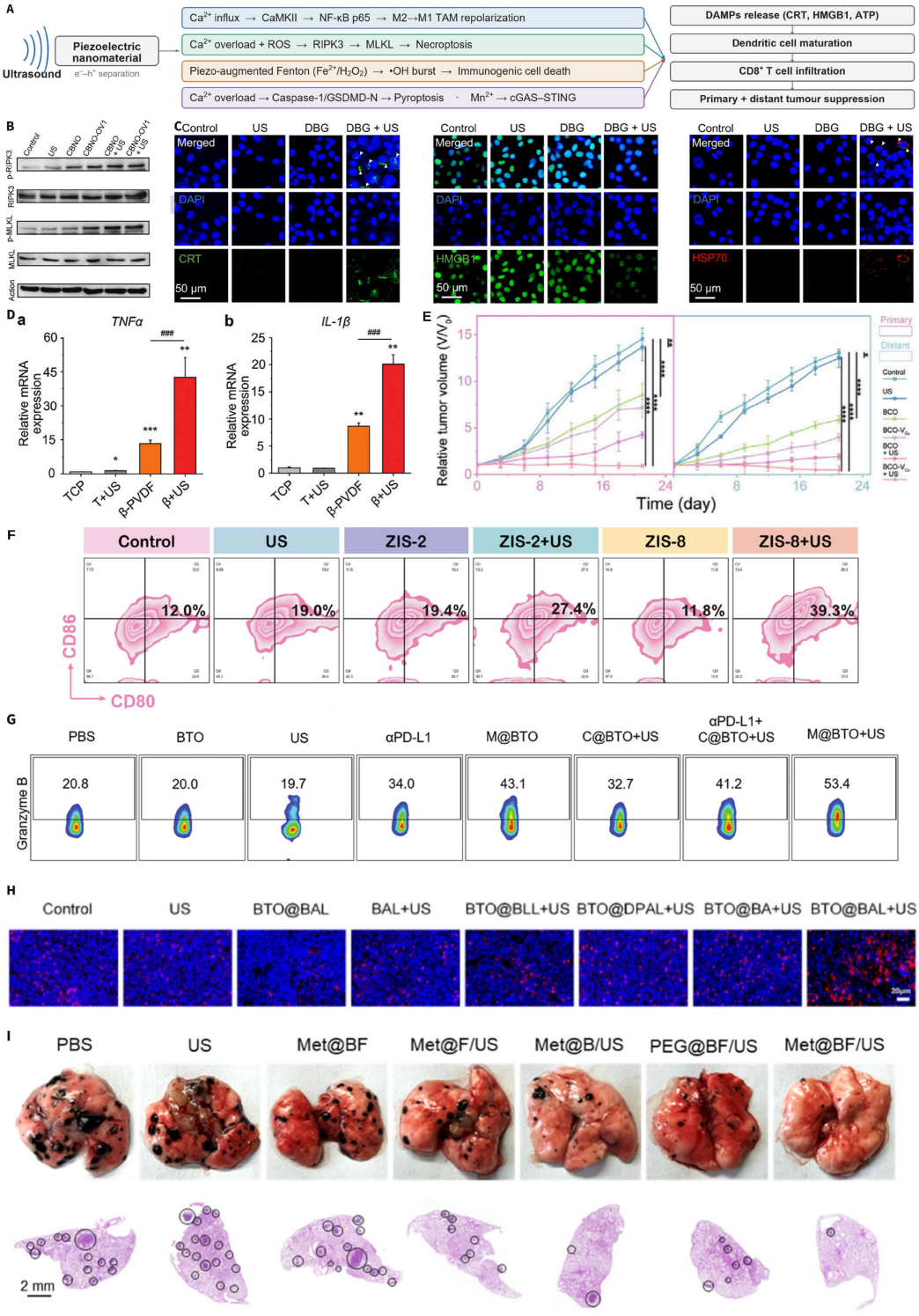


Figure 7. Signaling pathways and experimental evidence of piezoelectric immunoengineering. (A) Under ultrasound, piezocatalysis and piezoelectric stimulation converge on four pathways that convert a local reactive- oxygen input into systemic antitumor immunity: Ca^{2+}–CaMKII–NF-κB-driven M2→M1 repolarization of tumor-associated macrophages; Ca^{2+}/ROS-triggered RIPK3–MLKL necroptosis; piezo-augmented Fenton chemistry driving immunogenic cell death; and Ca^{2+} overload- plus Mn^{2+}-mediated caspase-1/GSDMD pyroptosis with cGAS–STING activation. All four converge on DAMPs release, dendritic cell maturation, $CD8^+$ T cell infiltration and suppression of primary and distant tumors. Created in BioRender. T. (2026) https://BioRender.com/rfeeene. **(B)** Western blot of p-RIPK3/RIPK3 and p-MLKL/MLKL in CT26 cells treated with oxygen-vacancy- engineered $CaBi_2Nb_2O_9$ (CBNO-OV1) nanosheets under ultrasound, confirming activation of the necroptosis pathway. Adapted with permission from Ref. [148]. Copyright 2023 Wiley-VCH GmbH. **(C)** Immunofluorescence of calreticulin (CRT) exposure, HMGB1 release and HSP70 expression in 4T1 cells treated with 2-

deoxyglucose-loaded $BiFeO_3$ (DBG) nanosheets, showing hallmarks of immunogenic cell death. Adapted with permission from Ref. [156]. Copyright 2024 the authors. **(D)** Relative mRNA expression of the M1 markers TNF-α and IL-1β in macrophages cultured on β-PVDF films with or without ultrasound. Adapted with permission from Ref. [150]. Copyright 2021 the authors. **(E)** Relative growth curves of primary and distal tumors in bilateral tumor-bearing mice treated with copper-vacancy Bi_2CuO_4 (BCO-V_{Cu}). Adapted with permission from Ref. [152]. Copyright 2024 Wiley-VCH GmbH. **(F)** Flow cytometry of $CD80^+CD86^+$ mature dendritic cells in tumor-draining lymph nodes of mice treated with sulfur-vacancy-optimized $ZnIn_2S_4$ (ZIS) nanosheets. Adapted with permission from Ref. [90]. Copyright 2025 Wiley-VCH GmbH. **(G)** Flow cytometry of Granzyme B^+ cells among intratumoral $CD8^+$ T cells in B16F10-bearing mice treated with MMP2-activated cell-membrane-coated $BaTiO_3$ (M@BTO) nanoparticles. Adapted with permission from Ref. [149]. Copyright 2023 Wiley-VCH GmbH. **(H)** Immunofluorescence of intratumoral $CD8^+$ T cells in KPC pancreatic tumors treated with BTO@BAL nanoparticles. Adapted with permission from Ref. [154]. Copyright 2025 American Chemical Society. **(I)** Photographs and H&E staining of pulmonary metastatic nodules from B16F10-bearing mice treated with Met@BF nanohybrids. Adapted with permission from Ref. [159]. Copyright 2024 American Chemical Society.

Table 5. Candidate Materials for Clinical Translation

Material	d_{33} Range	Biodegradability	Regulatory Status	Primary Safety Risk	Recommended Application Scenario
$BaTiO_3$	~190 pC/N (bulk)	Non-biodegradable	No clinical data	Ba^{2+} leaching, nephrotoxicity	*In vitro* validation, mechanistic studies
ZnO	~12 pC/N	Slow dissolution	Precedent in topical formulations	Excess Zn^{2+} release, cytotoxicity	Surface coatings, wound dressings
PVDF	~20-30 pC/N (film)	Non-biodegradable	Precedent in implants such as sutures	Long-term *in vivo* retention, chronic inflammation	Sensors, energy harvesting
PLLA/PLGA	~5-10 pC/N	Fully biodegradable (lactic acid)	Numerous approved implants	Low piezoelectric coefficient, degradation rate control	Bone/cartilage regeneration scaffolds
Silk fibroin	<5 pC/N	Fully biodegradable	Approved for surgical sutures, etc.	Extremely low piezoelectric coefficient	Flexible implantable devices (long-term)
HfO_2	Modest piezoresponse in the monoclinic phase; enhanced by phase stabilization or doping	Non-biodegradable	NBTXR3 has completed phase II-III clinical trials [172]	Long-term retention (but safety data have accumulated)	Reference platform for doped derivatives
Mn-doped HfO_2	Piezocatalytically active after doping	Non-biodegradable	No clinical data; HfO_2 data serve only as a reference baseline; likely regulated as a drug-device combination	Mn ion leaching, hepatorenal burden	Anti-infective implant coating, tumor therapy [92]

Determining whether abscopal responses stem from piezocatalytic immune priming or from the co-administered immunotherapy requires a factorial design in matched bilateral tumor models with six groups: vehicle, ultrasound alone, material alone, material plus ultrasound, checkpoint inhibitor alone (e.g., anti-PD-1 or anti-PD-L1), and the full combination. Each comparison answers a defined question. Material plus ultrasound against material alone and ultrasound alone isolates the piezocatalytic effect on the treated tumor. The same comparison read on the untreated distant tumor, in the absence of any checkpoint inhibitor, tests whether piezocatalysis by itself primes a systemic response. The full combination against checkpoint inhibitor alone measures the added value of piezocatalysis, and its comparison with the Bliss-independent expectation derived from material plus ultrasound and checkpoint inhibitor alone separates synergy from additivity, following the criteria in Section 6.2. Replacing the material with a compositionally matched non-piezoelectric counterpart further separates piezoelectricity from material chemistry (Section 9.3). Distant tumor growth should be read together with tumor antigen-specific T cell responses in draining lymph nodes and distant tumors, and $CD8^+$ T cell depletion shows whether the abscopal effect is T cell dependent.

The central question in piezoelectric immunoengineering shifts from 'how high is the ROS yield' to 'how does the spatiotemporal pattern of ROS act on specific immune cells' [145]. This shift imposes new requirements on materials design: different modes of cell death (pyroptosis, necroptosis, ferroptosis) differ in immunogenicity, so materials must control the species, dose, and subcellular localization of ROS to selectively trigger a specific death pathway [45,148,152,158]. At the same time, piezocatalysis plays a local-input role within combination immunotherapy, while the systemic immune effect is determined mainly by the co-administered immune drug or immune cells. Current studies generally lack a complete control design capable of isolating the independent immune contribution of piezocatalysis [145,153,156].

9. Clinical translation bottlenecks and roadmap

9.1 Long-term *in vivo* retention and potential toxicity

Commonly used piezocatalytic materials such as $BaTiO_3$ and PVDF degrade slowly or not at all *in vivo* and can lead to chronic inflammation with long-term exposure [1,2]. Ba-containing systems also leach barium ions, which cause nephrotoxicity [161]. Long-term data on Bi-containing systems are lacking [162]. The potential for off-target oxidative damage to cells, resulting from Fenton reactions, should also be

considered for Cu and Fe-containing systems. Most studies evaluate the effects of these materials through major organ H&E staining and blood biochemistry over a 7 to 30 day time course [1,2,163].

The clearance mechanism and rate of elimination of piezocatalytic nanoparticles depends significantly upon the particle size, or more specifically, the hydrodynamic diameter. For example, particles having a hydrodynamic diameter less than about 5.5 nm will be eliminated rapidly through the kidneys, which has been shown with quantum dots [164], with a urine elimination half-life that typically occurs within hours. Particles having a hydrodynamic diameter of 10-100 nm will primarily accumulate in the reticuloendothelial system (i.e. liver and spleen) and will have an elimination half-life ranging from days to weeks based on both the type of surface treatment applied to the particles and the composition of the particles themselves [165]. Because most piezocatalytic nanoparticles have a hydrodynamic diameter between 50-500 nm, they will be eliminated slowly from the body via hepatic/splenic elimination mechanisms. One approach to reducing the time required for elimination of piezocatalytic nanoparticles is to utilize biodegradable alternative forms of piezoelectric materials. For example, biodegradable piezoelectric scaffolds composed of PLLA or PLGA will degrade into lactic acid over several weeks or months and have a long history of safe use. Additionally, ZnO will dissolve into Zn^{2+} ions that can then be incorporated into normal metabolic processes related to zinc at lower concentrations. Lastly, bio-piezoelectric scaffolds composed of peptide or polysaccharide assemblies provide fully resorbable scaffold structures that exhibit lower piezoelectric properties than traditional piezoelectric materials. Conversely, non-degradable piezoelectric scaffolds composed of PVDF will persist in the body for extended periods of time and are designed to provide structural support for implants that require long-term stability.

Retention risk can be decreased in two ways. The first relies on a fully fast-resorbable polymer, such as PLLA and PLGA, which degrade to lactic acid and are considered safe. While 3D printing and electrospinning can enhance the piezoresponsive behavior of these materials, the currently measurable piezoelectric d_{33} (5 to 10 pC/N) is far less than that of $BaTiO_3$ [122,166]. PLLA piezoelectric scaffolds have been able to induce intra-articular cartilage regeneration in rabbits providing the first *in vivo* evidence for a fast-resorbable piezoelectric scaffold [111,122]. The second relies on biocompatible and fully resorbable polymers [167]. Silk fibroin and supramolecular piezoresponsive polymers undergo controlled degradation; however, their piezoelectric coefficients remain low and further optimization is needed [168,169].

A large amount of clinical safety information has accumulated for NBTXR3, which have been evaluated in Phase II–III clinical trials as a radiosensitizer to treat soft tissue sarcomas. However, it should be noted that the clinical safety information that has been compiled on unmodified NBTXR3 cannot simply be applied to Mn-doped HfO_2 piezocatalytic materials. The gap is structural as well as toxicological. Pristine monoclinic HfO_2 shows only a modest piezoresponse, and strong piezocatalytic activity appears only after a non-centrosymmetric phase is stabilized or aliovalent dopants such as Mn are introduced. NBTXR3 acts as an inert physical radioenhancer, whereas Mn-doped HfO_2 releases variable-valence Mn ions and exerts enzyme-like and glutathione-depleting activity [92]. These features change the toxicological profile and ion-leaching kinetics, and they move the material from the device category under which NBTXR3 was assessed toward a metabolically active or combination drug-device product with its own regulatory pathway. As such, Mn-doped HfO_2 must undergo its own separate preclinical safety evaluations, although the safety data obtained on NBTXR3 can serve as a baseline for comparisons. Of the materials discussed here, PLLA, whose piezoelectric form shares the chemistry of approved implants, appears closest to translation, followed by HfO_2, whose regulatory precedent covers only the undoped radioenhancer (Table 5).

The MIRIBEL recommendations [170] and the ARRIVE 2.0 guidelines [171] provide reporting standards for nanomaterials used in innovative therapeutic approaches. The MIRIBEL recommendations include three levels of reporting standards for reporting physicochemical characterization, biological evaluations, and experimental designs. Minimum reporting standards for animal experiments are provided by the ARRIVE 2.0 guidelines. Most of the studies referenced in this review did not sufficiently report essential elements listed in the MIRIBEL recommendations including quantitative information on the colloidal stability in biological systems, protein corona development [73] and *in-vivo* distribution [164,165].

9.2 Indiscriminate oxidation by ROS

Ultrasound generates scattered and reflected sound waves when interacting with biological tissue. This can cause unintended oxidative damage to the healthy tissue around the lesion when piezoelectric material is distributed there [4].

The design responsive to the microenvironment can counter this issue. Tumors have low pH, high

GSH, and high H_2O_2 levels, and these differences can be used to achieve selective catalytic activation. Within the BCO-V_{Cu} system, the Cu part releases Cu^+ in the acidic microenvironment to trigger a Fenton-like reaction, and piezocatalysis generates H_2O_2 while also depleting GSH to lower the antioxidant defense of the tumor cells; normal tissue with neutral pH and lower GSH does not trigger this cascade [152]. pH-controlled drug release, GSH-controlled carrier degradation, and enzyme-controlled interfacial site activation have been observed in many systems [149,159,173]. The synergy of piezocatalysis with nanozymes can spatially limit the ROS generation, which will subsequently reduce the unwanted impact on normal tissue [37,174,175].

9.3 Absence of a standardized evaluation system

The piezocatalysis literature lacks standards for ultrasound parameters, ROS detection, and the design of control groups. As such, the performance data of the cited works remains incommensurable [176].

When reporting ultrasound dose, frequency and nominal power are commonly stated; however, critical parameters such as duty cycle, probe-to-sample distance, container geometry, and medium attenuation coefficients are often omitted. ter Haar [177] and Padilla et al. [178] devised separate frameworks of tiered reporting for bioeffects and clinical ultrasound research, respectively, and the application of such to the field of piezocatalysis would not require any new and/or original research.

For ROS detection, Murphy et al. [179] set the consensus standards for cellular and *in vivo* studies to measure ROS in Nature Metabolism.

In EPR studies, spin trapping methods can rank order results in certain experiments, but signal intensities cannot be compared across experiments. 2′,7′-dichlorodihydrofluorescein diacetate (DCFH-DA) as a fluorescent probe is not selective and may react with several oxidizing species [179,180]. Isotope labeling with $H_2{}^{18}O$ and $^{18}O_2$ could be used to differentiate the piezocatalytic mechanism from the sonochemical mechanism. Comparing ROS output before and after cavitation is suppressed, for example by degassing the medium or raising the static pressure, can further estimate the sonochemical share.

Most studies include only a blank group and a no-ultrasound group as controls. They lack a compositionally matched non-piezoelectric control (for example, heat treated to remove polarization, or a centrosymmetric isomorph) and a dose-matched co-catalytic-component control (the free metal ions must be in the same concentration) [4,181-183]. In the absence of the former mentioned, piezoelectric effects and sonochemical effects cannot be differentiated. Without the latter, the contributions of piezocatalysis and Fenton-like reactions cannot be separated.

9.4 Translation pathways by product type

Differentiation is needed in the translation pathway for the three product forms, as each faces key issues and regulatory routes that are distinct and specific.

Out of all product forms, wound hydrogels and patches have materials with the most advanced state of evidence toward translation. There are still key issues to be addressed with respect to their safety in extraction and their stability in degrading and in storage. A gel bandage with piezoelectric and low intensity ultrasound focus has been tested in a diabetic-wound model providing good longitudinal data for *in vivo* uses [123]. However, it is necessary to validate large animal models and adjust the clinical use of ultrasound. This category of products should be assessed for the effectiveness of standard dressings and electrical stimulators.

Implant coatings, such as anti-infection surfaces for orthopedic hardware, present specific translational challenges regarding adhesion strength, wear fatigue, particle shedding, and compatibility with sterilization protocols.

Doped HfO_2 thin films can provide uniform surface coverage of implants through atomic layer deposition (ALD); NBTXR3 data can serve only as a reference baseline, as thin films differ from nanoparticles in composition, dose, exposure route, and degradation. A piezoelectric sensor-based "smart" spinal fusion implant, which does not involve piezocatalysis, has been designated an FDA Breakthrough Device (and sets the baseline for the other products). Products in this category should be compared to standard bone cement and antibiotics.

Of all possible combinations of injectable nanoparticles and ultrasonic equipment, the largest number of translational variables exists. The higher the acoustic frequency, the greater the attenuation. Attenuation of the acoustic wave as it passes through deep or fluid-filled bone cavities causes a significant decrease in acoustic pressure at the site of treatment. Most animal experiments employ subcutaneous tumor models. Because the acoustic path to these superficial tumors is unobstructed, such models underestimate the difficulty of treating deep-seated solid tumors, where the acoustic path is obstructed. Although some animal experiments utilize orthotopic pancreatic cancer models, measurements of acoustic pressures within the clinical setting during treatment remain to be determined. From a materials standpoint, once particles have been injected into the body, they will immediately begin to attach proteins to their surfaces.

This attachment will create a protein "corona," which will alter the surface chemistry of the particle and its effective size [73]. The amount of particles that ultimately reach the desired tissue site after being propelled via circulation is dependent upon the enhanced permeability and retention effect and/or active targeting mechanisms. Both mechanisms are currently under debate [164,165]. Efficacy-wise, this product category should be evaluated against other clinical sonodynamic therapies and ablation/radiotherapy treatments.

There is a total lack of systematic manufacturing data for all three product categories. Batch-to-batch reproducibility, sterilization tolerance, and storage stability for preclinical assessment of nanomedicines are accepted. However, there is currently no data tracking if defect states retain their original concentration post-sterilization, and if the strength of the polarization field decays during storage [1,163].

10. Future perspectives

10.1 Systematic comparison of defect engineering and high-d_{33} strategies

Within their respective studies, defect engineering increased the ROS yield of O_v-BOS approximately ten-fold, and the $BaTiO_3$@TiO_{2-x} heterojunction showed a rate constant of 7.8 times that of the bare $BaTiO_3$ under combined light and ultrasound. Furthermore, $Bi_4Ti_3O_{12}$ nanosheets, on the other hand, with surface oxygen vacancies and corona poling, display post-processing an excellent enhancement of the sono-piezocatalytic performance. These within-study comparisons suggest that charge utilization, in addition to charge generation, can limit catalytic activity, although the two systems cannot be compared directly because their test conditions differ. Unfortunately, there is wide variability in the numerous studies of the same field, hence why the results are primarily qualitative. Therefore, if and when the mixed technologies of defect engineering and high-d_{33} are implemented into case studies, a firm consensus among practitioners in the field might be reached.

10.2 Translation potential of approved material platforms

The slow progression of engineered piezo-catalytic nanomedicine into clinical trials is likely a result of a lack of long-term safety data. Adopting material platforms that already possess regulatory safety data may shorten the translation timeline.

The clinical use of HfO_2 is the most advanced. NBTXR3 has completed Phase II–III RCTs for soft tissue sarcomas. These trials demonstrated that NBTXR3 was both safe and effective at enhancing the effects of radiation therapy [172]. Doping HfO_2 with Mn can facilitate the synthesis of multi-enzyme activity and piezocatalytic activity [92]. Although there are several years worth of human-phase clinical safety data available on HfO_2, providing a starting point for moving from radiosensitization to piezocatalysis would require independent preclinical validation of the doped formulation. PLLA degrades to lactic acid, which has extensive safety data. PLLA piezoelectric scaffolds were successful in inducing cartilage regeneration in rabbits' knees [122]. Conducting long-term safety studies (longer than six months) on larger animals to determine histopathology, blood biochemistry, and substance accumulation in organs is the logical next step for each path [170,171]. An example of regulatory support for piezoelectric devices can be seen when the FDA awarded Breakthrough Device Designation to one of the piezoelectric-sensor smart implants.

10.3 Standardized databases and data-driven materials design

The main difficulty in comparison across many studies is the lack of standard data. The CatTestHub database in the field of heterogeneous catalysis has more than 250 data entries across 24 catalysts and 3 families of probe reactions, and is in line with the FAIR principles [184]. A similar approach could be used in designing a piezocatalysis database, where data owners would have to provide specifications of the materials and measured output under agreed benchmark conditions, and would be obliged to provide the full set of ultrasound parameters and the methods of detection [177,178].

The design of piezocatalysts using machine learning has progressed to some extent. He et al. [21] utilized machine learning to enhance the discovery process for optimized piezocatalysts in ceramic systems based on barium titanate. Wu et al. utilized a high throughput first-principle screening approach to identify $NbOI_2$, an example of a layer that exhibited high piezoelectric potential, from the 2940 monolayer materials [74]. Moving forward, the intricate, nonlinear relationships between structure and function within piezocatalysis (including, but not limited to; composition, defect concentration, morphology, ultrasound parameters, and biological outcomes) will necessitate the development of more advanced, data-driven strategies. Gradient boosting methods (e.g., XGBoost, LightGBM) are particularly effective at dealing with tabular data sets that are common in materials science. For image-related input types (e.g., electron micrographs, crystal structures, spatial maps of defects), both convolutional neural

networks (CNNs) and graph neural networks have the ability to generate features that would be challenging to develop manually. Transformer architectures appear to have significant potential for the integration of multiple modalities of data (e.g., spectra, images, tabular features) into a single predictive model. Ultimately, the combination of these architectures with least absolute shrinkage and selection operator (LASSO)-based feature selection and SHapley Additive exPlanations (SHAP)-based model interpretation may significantly speed up the transition from empirical screening to a rational, data-driven method for developing piezocatalytic nanomedicines.

The three directions listed above are the examples of an advancement relationship. Once a standardized database is established, high-d_{33} and defect engineering can be compared in a systematic way, which will allow the selection of translation choices in the authorized material platforms.

11. Conclusion

There are many challenges to achieving high efficiency in piezocatalytic nanomedicine. These challenges include, but are not limited to, the bulk electron-hole recombination rate, the ultrasound settings used, the rate at which reactions take place at the surface of the catalyst, and the biological environment in which the nanomedicine operates. There are several strategies to reduce the impact of the bulk electron-hole recombination rate. For example, researchers can engineer heterojunctions, create defects, or develop piezoelectric hydrogels. All three approaches allow researchers to address the bulk electron-hole recombination issue in terms of spatial, temporal, and catalytic-medium dimensions. Each of these three approaches can be combined into a single system. The clinically oriented decision tree proposed in this review can serve as a basis for selecting which materials should be utilized (i.e., HfO_2 vs. PLLA). Additionally, it can guide researchers in identifying the most mature technologies. Breakthroughs in the development of systems will consolidate work performed across three distinct areas: standardizing evaluation systems will enable comparative analysis across different studies; capturing safety information regarding existing material systems will enable researchers to test on large animal models; and standardizing data will enable researchers to utilize data-driven design methods for developing new materials.

Abbreviations

ALD: Atomic Layer Deposition; **ARRIVE:** Animal Research: Reporting of *In vivo* Experiments; **BOS:** $Bi_2O_2SiO_3$ (Bismuth Oxysilicate); **BMO:** Bi_2MoO_6 (Bismuth Molybdate); **BTO:** $BaTiO_3$ (Barium Titanate); **CAF:** Cancer-Associated Fibroblast; **CaM:** Calmodulin; **CaMKII:** Ca^{2+}/Calmodulin-Dependent Protein Kinase II; **cGAS:** Cyclic GMP-AMP Synthase; **CNN:** Convolutional Neural Network; **CRT:** Calreticulin; **d_{33}:** Piezoelectric Charge Coefficient; **DAMPs:** Damage-Associated Molecular Patterns; **DCFH-DA:** 2',7'-Dichlorodihydrofluorescein Diacetate; **DFT:** Density Functional Theory; **EELS:** Electron Energy Loss Spectroscopy; **EIS:** Electrochemical Impedance Spectroscopy; **EPR:** Electron Paramagnetic Resonance; **FAIR:** Findable, Accessible, Interoperable, Reusable; **FDA:** Food and Drug Administration; **GAGs:** Glycosaminoglycans; **GSDMD:** Gasdermin D; **GSH:** Glutathione; **H&E:** Hematoxylin and Eosin; **HMGB1:** High Mobility Group Box 1; **HOMO:** Highest Occupied Molecular Orbital; **ICD:** Immunogenic Cell Death; **IL-1β:** Interleukin-1β; **LASSO:** Least Absolute Shrinkage and Selection Operator; **LIFU:** Low-Intensity Focused Ultrasound; **LIPUS:** Low-Intensity Pulsed Ultrasound; **LUMO:** Lowest Unoccupied Molecular Orbital; **MI:** Mechanical Index; **MIRIBEL:** Minimum Information Reporting in Bio-Nano Experimental Literature; **MLKL:** Mixed Lineage Kinase Domain-Like Pseudokinase; **MMP2:** Matrix Metalloproteinase 2; **MRSA:** Methicillin-Resistant Staphylococcus aureus **NBTXR3:** Hafnium Oxide Nanoparticle (Clinical Radiosensitizer); **NF-κB:** Nuclear Factor Kappa-Light-Chain-Enhancer of Activated B Cells; **NR:** Not Reported in the main text of the original study; **OHA:** Oxidized Hyaluronic Acid; **O_v:** Oxygen Vacancy; **PEDOT:PSS:** Poly(3,4-ethylenedioxythiophene):Poly (styrene sulfonate); **PEG:** Poly(ethylene glycol); **PJTE:** Pseudo-Jahn-Teller Effect; **PLGA:** Poly(lactic-co-glycolic acid); **PLLA:** Poly(L-lactic acid); **PVA:** Poly(vinyl alcohol); **PVDF:** Poly(vinylidene fluoride); **RhB:** Rhodamine B; **RIPK3:** Receptor-Interacting Serine/Threonine-Protein Kinase 3; **ROS:** Reactive Oxygen Species; **SHAP:** SHapley Additive exPlanations; **STEM:** Scanning Transmission Electron Microscopy; **STING:** Stimulator of Interferon Genes; **THM:** N-[Tris(hydroxymethyl)methyl]acrylamide; **TNF-α:** Tumor Necrosis Factor-α; **TRP:** Transient Receptor Potential; **XPS:** X-ray Photoelectron Spectroscopy.

Acknowledgements

Funding

Liaoning Provincial Natural Science Foundation Project in 2025 (No. 2025-MS-184); National Natural Science Foundation of China Youth Project (No. 82502391, No.82603846).

Author contributions

Conceptualisation, C.Z., B.Z. and H.T.; methodology, C.Z. and H.T.; validation, C.Z., B.Z. and H.T.; investigation, H.T., W.Y., W.Z., W.G. and L.Y.; data curation, H.T., W.Y. and W.Z.; writing, original draft preparation, H.T. and C.Z.; writing, review and editing, C.Z., B.Z., H.T., W.G. and L.Y.; visualisation, H.T., W.Y. and W.Z.; supervision, C.Z. and B.Z.; project administration, C.Z. All authors have read and agreed to the published version of the manuscript.

Competing Interests

The authors have declared that no competing interest exists.

References

1. Chen S, Zhu P, Mao L, Wu W, Lin H, Xu D, et al. Piezocatalytic medicine: an emerging frontier using piezoelectric materials for biomedical applications. Adv Mater. 2023; 35: e2208256.
2. Cafarelli A, Marino A, Vannozzi L, Puigmartí-Luis J, Pané S, Ciofani G, et al. Piezoelectric nanomaterials activated by ultrasound: the pathway from discovery to future clinical adoption. ACS Nano. 2021; 15: 11066-86.
3. Wang X, Dai X, Chen Y. Sonopiezoelectric nanomedicine and materdicine. Small. 2023; 19: e2301693.
4. Chen Z, Sang L, Liu Y, Bai Z. Sono-piezo dynamic therapy: utilizing piezoelectric materials as sonosensitizer for sonodynamic therapy. Adv Sci (Weinh). 2025; 12: e2417439.
5. Liang S, Deng X, Ma P, Cheng Z, Lin J. Recent advances in nanomaterial-assisted combinational sonodynamic cancer therapy. Adv Mater. 2020; 32: 2003214.
6. Wells PNT. Ultrasound imaging. Phys Med Biol. 2006; 51: R83-98.
7. He F, Li W, Liu B, Zhong Y, Jin Q, Qin X. Progress of piezoelectric semiconductor nanomaterials in sonodynamic cancer therapy. ACS Biomater Sci Eng. 2024; 10: 298-312.
8. Zhu P, Chen Y, Shi J. Piezocatalytic tumor therapy by ultrasound-triggered and BaTiO3-mediated piezoelectricity. Adv Mater. 2020; 32: e2001976.
9. Li Z, Zhang T, Fan F, Gao F, Ji H, Yang L. Piezoelectric materials as sonodynamic sensitizers to safely ablate tumors: a case study using black phosphorus. J Phys Chem Lett. 2020; 11: 1228-38.
10. Sengupta D, Naskar S, Mandal D. Reactive oxygen species for therapeutic application: role of piezoelectric materials. Phys Chem Chem Phys. 2023; 25: 25925-41.
11. Zheng H, Wang Y, Liu J, Wang J, Yan K, Zhu K. Recent advancements in the use of novel piezoelectric materials for piezocatalytic and piezo-photocatalytic applications. Appl Catal B Environ. 2024; 341: 123335.
12. Tu S, Guo Y, Zhang Y, Hu C, Zhang T, Ma T, et al. Piezocatalysis and piezo-photocatalysis: catalysts classification and modification strategy, reaction mechanism, and practical application. Adv Funct Mater. 2020; 30: 2005158.
13. Hong KS, Xu H, Konishi H, Li X. Direct water splitting through vibrating piezoelectric microfibers in water. J Phys Chem Lett. 2010; 1: 997-1002.
14. Meng N, Liu W, Jiang R, Zhang Y, Dunn S, Wu J, et al. Fundamentals, advances and perspectives of piezocatalysis: a marriage of solid-state physics and catalytic chemistry. Prog Mater Sci. 2023; 138: 101161.
15. Liu J, Qi W, Xu M, Thomas T, Liu S, Yang M. Piezocatalytic techniques in environmental remediation. Angew Chem Int Ed Engl. 2023; 62: e202213927.
16. Wang C, Hu C, Chen F, Ma T, Zhang Y, Huang H. Design strategies and effect comparisons toward efficient piezocatalytic system. Nano Energy. 2023; 107: 108093.
17. Starr MB, Wang X. Fundamental analysis of piezocatalysis process on the surfaces of strained piezoelectric materials. Sci Rep. 2013; 3: 2160.
18. Wang K, Han C, Li J, Qiu J, Sunarso J, Liu S. The mechanism of piezocatalysis: energy band theory or screening charge effect? Angew Chem Int Ed Engl. 2022; 61: e202110429.
19. Jin CC, Ai JD, Liu DM, Tan LN, Cao L, Shen BL, et al. Significantly enhanced piezocatalytic activity of BaTiO3 by regulating the quenching process. J Mater Chem A. 2023; 11: 10360-70.
20. Wu J, Xu Q, Lin E, Yuan B, Qin N, Thatikonda SK, et al. Insights into the role of ferroelectric polarization in piezocatalysis of nanocrystalline BaTiO3. ACS Appl Mater Interfaces. 2018; 10: 17842-9.
21. He J, Yu C, Hou Y, Su X, Li J, Liu C, et al. Accelerated discovery of high-performance piezocatalyst in BaTiO3-based ceramics via machine learning. Nano Energy. 2022; 97: 107218.
22. Ma J, Miao TJ, Tang J. Charge carrier dynamics and reaction intermediates in heterogeneous photocatalysis by time-resolved spectroscopies. Chem Soc Rev. 2022; 51: 5777-94.
23. Wilson AA, Hart L, Shalvey T, Sachs M, Xu W, Moss B, et al. Transient absorption spectroscopy reveals that slow bimolecular recombination in SrTiO3 underpins its efficient photocatalytic performance. Chem Commun (Camb). 2023; 59: 13579-82.
24. Low J, Yu J, Jaroniec M, Wageh S, Al-Ghamdi AA. Heterojunction photocatalysts. Adv Mater. 2017; 29: 1601694.
25. Dong H, Zhou Y, Wang L, Chen L, Zhu M. Oxygen vacancies in piezocatalysis: a critical review. Chem Eng J. 2024; 487: 150480.
26. Wang P, Tang Q, Zhang L, Xu M, Sun L, Sun S, et al. Ultrasmall barium titanate nanoparticles for highly efficient hypoxic tumor therapy via ultrasound triggered piezocatalysis and water splitting. ACS Nano. 2021; 15: 11326-40.
27. Bößl F, Comyn TP, Cowin PI, García-García FR, Tudela I. Piezocatalytic degradation of pollutants in water: importance of catalyst size, poling and excitation mode. Chem Eng J Adv. 2021; 7: 100133.
28. Xu Q, Zhang L, Cheng B, Fan J, Yu J. S-scheme heterojunction photocatalyst. Chem. 2020; 6: 1543-59.
29. Liu Q, Zhai D, Xiao Z, Tang C, Sun Q, Bowen CR, et al. Piezo-photoelectronic coupling effect of BaTiO3@TiO2 nanowires for highly concentrated dye degradation. Nano Energy. 2022; 92: 106702.
30. Xue J, Fujitsuka M, Tachikawa T, Bao J, Majima T. Charge trapping in semiconductor photocatalysts: a time- and space-domain perspective. J Am Chem Soc. 2024; 146: 8787-99.
31. Bai S, Zhang N, Gao C, Xiong Y. Defect engineering in photocatalytic materials. Nano Energy. 2018; 53: 296-336.
32. Zhang C, Kwon SH, Dong L. Piezoelectric hydrogels: hybrid material design, properties, and biomedical applications. Small. 2024; 20: e2310110.
33. Vijayakanth T, Shankar S, Finkelstein-Zuta G, Rencus-Lazar S, Gilead S, Gazit E. Perspectives on recent advancements in energy harvesting, sensing and bio-medical applications of piezoelectric gels. Chem Soc Rev. 2023; 52: 6191-220.
34. Bößl F, Menzel VC, Jeronimo K, Arora A, Zhang Y, Comyn TP, et al. Importance of energy band theory and screening charge effect in piezo-electrocatalytical processes. Electrochim Acta. 2023; 462: 142730.
35. Wang L, Zhu K, Guo J, Li X, Zheng H, Li Z, et al. Piezo-photocatalysis enhanced by modulation of oxygen vacancies in BaTiO3@TiO2-x heterojunction. Appl Surf Sci. 2026; 737: 166902.
36. Dai J, Shao N, Zhang S, Zhao Z, Long Y, Zhao S, et al. Enhanced piezocatalytic activity of Sr0.5Ba0.5Nb2O6 nanostructures by engineering surface oxygen vacancies and self-generated heterojunctions. ACS Appl Mater Interfaces. 2021; 13: 7259-67.
37. Wang J, Wang J, Wang Z, Wu J, Liao J, Zhan S, et al. Piezocatalytic Pt@BMO-gel dressing for *in situ* generation of H2 and NO to treat infectious inflammation related to incontinence. Adv Funct Mater. 2026; 36: e22731.
38. Roy S, Fan Z, Ullah Z, Madni M, Shyamal S, Roy J, et al. Ultrasound-powered piezoelectric hydrogel enables dual piezodynamic-chemodynamic therapy and immunomodulation against bacteria-infected burn wounds. Nano Energy. 2025; 146: 111535.
39. Wang Y, Zang P, Yang D, Zhang R, Gai S, Yang P. The fundamentals and applications of piezoelectric materials for tumor therapy: recent advances and outlook. Mater Horiz. 2023; 10: 1140-84.
40. Sherrell PC, Fronzi M, Shepelin NA, Corletto A, Winkler DA, Ford M, et al. A bright future for engineering piezoelectric 2D crystals. Chem Soc Rev. 2022; 51: 650-71.
41. Hong KS, Xu H, Konishi H, Li X. Piezoelectrochemical effect: a new mechanism for azo dye decolorization in aqueous solution through vibrating piezoelectric microfibers. J Phys Chem C. 2012; 116: 13045-51.
42. Chiang CH, Yu CH, Lu YS, Yang YC, Lin YC, Chen HA, et al. Polarization-switchable electrochemistry of 2D layered Bi2O2Se bifunctional microreactors by ferroelectric modulation. Nano Lett. 2024; 24: 11012-9.
43. Xu Q, Gao X, Wen M, Liu Y, Li Y, Wei C, et al. Biocomputation with MnTiO3 piezoelectric enzymes for programed catalysis of tumor death. ACS Appl Mater Interfaces. 2022; 14: 28199-210.
44. Marino A, Battaglini M, De Pasquale D, Degl'Innocenti A, Ciofani G. Ultrasound-activated piezoelectric nanoparticles inhibit proliferation of breast cancer cells. Sci Rep. 2018; 8: 6257.
45. Li G, Dai X, Liu Y, Chen J, Yu W, Li P, et al. Alternating interlayered piezoelectric self-heterojunction boosts sono-piezocatalytic pyroptosis oncotherapy. Adv Mater. 2025; 37: e2508941.
46. Kang Y, Lei L, Zhu C, Zhang H, Mei L, Ji X. Piezo-photocatalytic effect mediating reactive oxygen species burst for cancer catalytic therapy. Mater Horiz. 2021; 8: 2273-85.
47. Kalhori H, Youssef AH, Ruediger A, Pignolet A. Competing contributions to the catalytic activity of barium titanate nanoparticles in the decomposition of organic pollutants. J Environ Chem Eng. 2022; 10: 108571.
48. Feng Y, Ling L, Wang Y, Xu Z, Cao F, Li H, et al. Engineering spherical lead zirconate titanate to explore the essence of piezo-catalysis. Nano Energy. 2017; 40: 481-6.
49. Zhou X, Liu J, Ali S, Shen B, Zhai J, Hedin N, et al. Efficient catalytic production of reactive oxygen species through piezoelectricity in bismuth sulfide rich in sulfur vacancies. Nano Lett. 2024; 24: 13153-61.
50. Gaur A, Porwal C, Sharma M, Chauhan VS, Vaish R, Kebaili I, et al. Effect of poling and porosity on BaTiO3 for piezocatalytic dye degradation. J Mater Sci Mater Electron. 2023; 34: 2099.
51. Wang K, Li B, Zhao C, Yuan S, Zhang C, Liang X, et al. A novel NiO/BaTiO3 heterojunction for piezocatalytic water purification under ultrasonic vibration. Ultrason Sonochem. 2023; 92: 106285.

52. Han G, Wang P, Zhang X, Wang Z, Yu H, Li Z, et al. Mechanistic insights into chemical bonded BaTiO3/MoS2 dual piezoelectric heterojunction for robust piezo-photocatalytic performance. J Colloid Interface Sci. 2025; 697: 137919.
53. Long J, Ren T, Han J, Li N, Chen D, Xu Q, et al. Heterostructured BiFeO3@CdS nanofibers with enhanced piezoelectric response for efficient piezocatalytic degradation of organic pollutants. Sep Purif Technol. 2022; 290: 120861.
54. Ning X, Jia D, Li S, Khan MF, Hao A. Construction of CuS/ZnO Z-scheme heterojunction as highly efficient piezocatalyst for degradation of organic pollutant and promoting N2 fixation properties. Ceram Int. 2023; 49: 21658-66.
55. Miao Y, Tian W, Han J, Li N, Chen D, Xu Q, et al. Oxygen vacancy-induced hydroxyl dipole reorientation in hydroxyapatite for enhanced piezocatalytic activity. Nano Energy. 2022; 100: 107473.
56. Wang Y, Wu JM. Effect of controlled oxygen vacancy on H2-production through the piezocatalysis and piezophototronics of ferroelectric R3c ZnSnO3 nanowires. Adv Funct Mater. 2020; 30: 1907619.
57. Yuan X, Shi J, Kang Y, Dong J, Pei Z, Ji X. Piezoelectricity, pyroelectricity, and ferroelectricity in biomaterials and biomedical applications. Adv Mater. 2024; 36: e2308726.
58. Xu J, Che H, Tang C, Liu B, Ao Y. Tandem fields facilitating directional carrier migration in van der Waals heterojunction for efficient overall piezo-synthesis of H2O2. Adv Mater. 2024; 36: e2404539.
59. Ruan X, Ding C, Cai H, Jiang R, Xu M, Meng D, et al. Bulk polarization fields and interfacial electron sink in MXene-modified iodine-doped Bi4Ti3O12 enhance piezocatalytic H2O2 generation. Nat Commun. 2026; 17: 3915.
60. Huang H, Tu S, Zeng C, Zhang T, Reshak AH, Zhang Y. Macroscopic polarization enhancement promoting photo- and piezoelectric-induced charge separation and molecular oxygen activation. Angew Chem Int Ed Engl. 2017; 56: 11860-4.
61. Luo H, Liu Z, Ma C, Zhang A, Zhang Q, Wang F. 2D/2D KNbO3/MoS2 heterojunctions for piezocatalysis: insights into interfacial electric-fields and reactive oxygen species. J Environ Chem Eng. 2023; 11: 111521.
62. Li H, Ma W, Zeng X, Liu S, Xiao L, Fang Z, et al. ZnO/CuO piezoelectric nanocatalysts for the degradation of organic pollutants. ACS Appl Nano Mater. 2023; 6: 21113-22.
63. Ai M, Peng Z, Li X, Idrees F, Zhang X, Zou JJ, et al. Piezoelectric-enhanced n-TiO2/BaTiO3/p-TiO2 heterojunction for highly efficient photoelectrocatalysis. Green Energy Environ. 2024; 9: 1466-76.
64. Zhao C, Cai L, Wang K, Li B, Yuan S, Zeng Z, et al. Novel Bi2WO6/ZnSnO3 heterojunction for the ultrasonic-vibration-driven piezocatalytic degradation of RhB. Environ Pollut. 2023; 319: 120982.
65. Hao P, Cao Y, Ning X, Chen R, Xie J, Hu J, et al. Rational design of CdS/BiOCl S-scheme heterojunction for effective boosting piezocatalytic H2 evolution and pollutants degradation performances. J Colloid Interface Sci. 2023; 639: 343-54.
66. Xu M, Lu M, Qin G, Wu X, Yu T, Zhang L, et al. Piezo-photocatalytic synergy in BiFeO3@COF Z-scheme heterostructures for high-efficiency overall water splitting. Angew Chem Int Ed Engl. 2022; 61: e202210700.
67. Zhao Z, Ling Q, Li Z, Yan K, Ding C, Chen P, et al. S-scheme BaTiO3/TiO2 heterojunctions: piezophotocatalytic degradation of norfloxacin. Sep Purif Technol. 2023; 308: 122928.
68. Liu W, Wang P, Ao Y, Chen J, Gao X, Jia B, et al. Directing charge transfer in a chemical-bonded BaTiO3@ReS2 Schottky heterojunction for piezoelectric enhanced photocatalysis. Adv Mater. 2022; 34: e2202508.
69. Wu Y, Song X, Zhou X, Song R, Tang W, Yang D, et al. Piezo-activated atomic-thin molybdenum disulfide/MXene nanoenzyme for integrated and efficient tumor therapy via ultrasound-triggered Schottky electric field. Small. 2023; 19: e2205053.
70. Zhang J, Dong Z, Xue C, Qu L, Zhao T, Fu Y, et al. Silver niobate/platinum piezoelectric heterojunction enhancing intra-tumoral infiltration of immune cells for transforming cold tumor into hot tumor. J Colloid Interface Sci. 2025; 690: 137303.
71. Xu W, Li K, Shen L, Liu X, Chen Y, Feng J, et al. Piezodeposition of metal cocatalysts for promoted piezocatalytic generation of reactive oxygen species and hydrogen in water. ChemCatChem. 2022; 14: e202200312.
72. Ning X, Hao A, Cao Y, Chen R, Xie J, Lu Z, et al. Construction of MXene/Bi2WO6 Schottky junction for highly efficient piezocatalytic hydrogen evolution and unraveling mechanism. Nano Lett. 2024; 24: 3361-8.
73. Monopoli MP, Åberg C, Salvati A, Dawson KA. Biomolecular coronas provide the biological identity of nanosized materials. Nat Nanotechnol. 2012; 7: 779-86.
74. Wu Y, Abdelwahab I, Kwon KC, Verzhbitskiy I, Wang L, Liew WH, et al. Data-driven discovery of high performance layered van der Waals piezoelectric NbOI2. Nat Commun. 2022; 13: 1884.
75. Kang Z, Lin E, Qin N, Wu J, Bao D. Bismuth vacancy-mediated quantum dot precipitation to trigger efficient piezocatalytic activity of Bi2WO6 nanosheets. ACS Appl Mater Interfaces. 2022; 14: 11375-87.
76. Liu DM, Zhang JT, Jin CC, Chen BB, Hu J, Zhu R, et al. Insight into oxygen-vacancy regulation on piezocatalytic activity of (Bi1/2Na1/2)TiO3 crystallites: experiments and first-principles calculations. Nano Energy. 2022; 95: 106975.
77. Ranjan A, Hsiao KY, Lin CY, Tseng YH, Lu MY. Enhanced piezocatalytic activity in Bi1/2Na1/2TiO3 for water splitting by oxygen vacancy engineering. ACS Appl Mater Interfaces. 2022; 14: 35635-44.
78. Zhu Q, Dar AA, Zhou Y, Zhang K, Qin J, Pan B, et al. Oxygen vacancies promoted piezoelectricity toward piezo-photocatalytic decomposition of tetracycline over SrBi4Ti4O15. ACS ES T Eng. 2022; 2: 1365-75.
79. Zhang D, Li Y, Wang P, Qu J, Zhan S, Li Y. Regulating spin polarization through cationic vacancy defects in Bi4Ti3O12 for enhanced molecular oxygen activation. Angew Chem Int Ed Engl. 2023; 62: e202303807.
80. Zhao R, Zhu H, Feng L, Zhu Y, Liu B, Yu C, et al. 2D piezoelectric BiVO4 artificial nanozyme with adjustable vanadium vacancy for ultrasound enhanced piezoelectric/sonodynamic therapy. Small. 2023; 19: e2301349.
81. Xu T, Song X, Chang M, Chen L, Xia L, Chen Y, et al. Dual vacancies-engineered two-dimensional sonocatalysts for ultrasound-augmented and PANoptosis-driven catalytic tumor nanotherapy. Interdiscip Mater. 2025; 4: 343-58.
82. Kong M, Li Y, Chen X, Tian T, Fang P, Zheng F, et al. Tuning the relative concentration ratio of bulk defects to surface defects in TiO2 nanocrystals leads to high photocatalytic efficiency. J Am Chem Soc. 2011; 133: 16414-7.
83. Fu C, Wu T, Sun G, Yin G, Wang C, Ran G, et al. Dual-defect enhanced piezocatalytic performance of C3N5 for multifunctional applications. Appl Catal B Environ. 2023; 323: 122196.
84. Yang Z, Yuan M, Liu B, Ma Z, Ma J, Ma X, et al. Dual-defect regulated g-C3N4 for piezoelectric catalytic tumor therapy with enhanced efficacy. Adv Mater. 2025; 37: e2412069.
85. Yang Z, Yuan M, Cheng Z, Liu B, Ma Z, Ma J, et al. Defect-repaired g-C3N4 nanosheets: elevating the efficacy of sonodynamic cancer therapy through enhanced charge carrier migration. Angew Chem Int Ed Engl. 2024; 63: e202401758.
86. Ma J, Yuan M, Yang Z, Ma Z, Zhang J, Li Z, et al. Surface oxygen vacancies and corona polarization of Bi4Ti3O12 nanosheets for synergistically enhanced sonopiezoelectric therapy. J Am Chem Soc. 2024; 146: 22348-59.
87. Wang C, Chen F, Hu C, Ma T, Zhang Y, Huang H. Efficient piezocatalytic H2O2 production of atomic-level thickness Bi4Ti3O12 nanosheets with surface oxygen vacancy. Chem Eng J. 2022; 431: 133930.
88. Yang L, Tian B, Xie Y, Dong S, Yang M, Gai S, et al. Oxygen-vacancy-rich piezoelectric BiO_{2-x} nanosheets for augmented piezocatalytic, sonothermal, and enzymatic therapies. Adv Mater. 2023; 35: e2300648.
89. Ma X, Ding B, Yang Z, Liu S, Liu Z, Meng Q, et al. Sulfur-vacancy-engineered two-dimensional Cu@SnS2-x nanosheets constructed via heterovalent substitution for high-efficiency piezocatalytic tumor therapy. J Am Chem Soc. 2024; 146: 21496-508.
90. Yang M, Ding B, Ma X, Li J, Han D, Liu S, et al. Multipath ROS storm and immune activation via sulfur vacancy-optimized ZnIn2S4 nanosheets for piezocatalytic tumor therapy. Angew Chem Int Ed Engl. 2025; 64: e202507502.
91. Liu Y, Wang Y, Zhen W, Wang Y, Zhang S, Zhao Y, et al. Defect modified zinc oxide with augmenting sonodynamic reactive oxygen species generation. Biomaterials. 2020; 251: 120075.
92. Zhong L, Guo X, Deng L, Wang X, He H, Wu N, et al. Dopant-regulated piezocatalysts evoke sonopiezoelectric and enzymatic PANoptosis for synergistic cancer therapy. Adv Sci (Weinh). 2025; 12: e2500406.
93. Wang K, Guo X, Han C, Liu L, Wang Z, Thomsen L, et al. Creation of piezoelectricity in quadruple perovskite oxides by harnessing cation defects and their application in piezo-photocatalysis. ACS Nano. 2025; 19: 3818-29.
94. Zheng Y, Dai Y, Lin Z, Li G, Zhang H, Xu J, et al. Piezoelectric nanozymes with acoustically rejuvenated catalytic activities rewire lipid metabolism for two-pronged ferroptotic therapy. Angew Chem Int Ed Engl. 2026; 65: e6613248.
95. Ning J, Kang Z, Qin N, Chen M, Wu J, Bao D. Boosting piezocatalytic performance of perovskite BiFeO3 with controlled oxygen vacancies. J Alloys Compd. 2024; 978: 173370.
96. Li X, Wang Y, Cao X, Song X, Chen L, Chang M, et al. Lanthanide-specific doping in vacancy-engineered piezocatalysts induces lysosomal destruction and tumor cell pyroptosis. J Nanobiotechnology. 2025; 23: 331.
97. Wang Y, Xu X, Xiao L, Li L, Xu Q, Wen Z, et al. Balancing the piezoelectric coefficient and carrier concentration of Bi_2WO_{6-x} for ultrahigh piezocatalysis. J Adv Ceram. 2024; 13: 1737-47.
98. Yang Z, Yuan M, Liu B, Zhang W, Maleki A, Guo B, et al. Conferring BiVO4 nanorods with oxygen vacancies to realize enhanced sonodynamic cancer therapy. Angew Chem Int Ed Engl. 2022; 61: e202209484.
99. Yu C, Dong Y, Zhu X, Feng L, Zang P, Liu B, et al. Oxygen vacancy piezoelectric nanosheets constructed by a photoetching strategy for ultrasound unlocked tumor synergistic therapy. Nano Lett. 2024; 24: 8008-16.
100. Miao TJ, Tang J. Characterization of charge carrier behavior in photocatalysis using transient absorption spectroscopy. J Chem Phys. 2020; 152: 194201.
101. Ran M, Du B, Liu W, Liang Z, Liang L, Zhang Y, et al. Dynamic defects boost in-situ H2O2 piezocatalysis for water cleanup. Proc Natl Acad Sci U S A. 2024; 121: e2317435121.
102. Cai L, Sun T, Han F, Zhang H, Zhao J, Hu Q, et al. Degradable and piezoelectric hollow ZnO heterostructures for sonodynamic therapy and pro-death autophagy. J Am Chem Soc. 2024; 146: 34188-98.
103. Li L, Shao Y, Jia L, Guo ZH, Li Z, Wang ZL, et al. A d33 piezoionic hydrogel with bioinspired multi-gradient structure for enhanced mechano-iontronic transduction. Nano Energy. 2025; 133: 110477.
104. Li X, Zhang T, Wang C, Qiao Z, Zhang Q, Wu S. Influence of cell force-driven piezoionic hydrogels on the migration of cancer cells. Nano Res. 2026; 19: 94908694.
105. Chen W, Zhang S, Zhang A, Liu H, Wu Z, Zhai L, et al. Intercellular ion-gradient piezoheterogated biphasic gel for ultrahigh iontronic generation. J Am Chem Soc. 2025; 147: 3283-92.
106. Fiumefreddo A, Utz M. Bulk streaming potential in poly(acrylic acid)/poly(acrylamide) hydrogels. Macromolecules. 2010; 43: 5814-9.

107. Liu D, Li L, Shi BL, Shi B, Li MD, Qiu Y, et al. Ultrasound-triggered piezocatalytic composite hydrogels for promoting bacterial-infected wound healing. Bioact Mater. 2023; 24: 96-111.
108. Wu M, Zhang Z, Liu Z, Zhang J, Zhang Y, Ding Y, et al. Piezoelectric nanocomposites for sonodynamic bacterial elimination and wound healing. Nano Today. 2021; 37: 101104.
109. Dobashi Y, Yao D, Petel Y, Nguyen TN, Sarwar MS, Thabet Y, et al. Piezoionic mechanoreceptors: force-induced current generation in hydrogels. Science. 2022; 376: 502-7.
110. Chen W, Zhou K, Wu Z, Yang L, Xie Y, Meng X, et al. Ion-concentration-hopping heterolayer gel for ultrahigh gradient energy conversion. J Am Chem Soc. 2024; 146: 13191-200.
111. Vinikoor T, Dzidotor GK, Le TT, Liu Y, Kan HM, Barui S, et al. Injectable and biodegradable piezoelectric hydrogel for osteoarthritis treatment. Nat Commun. 2023; 14: 6257.
112. Skovsen E, Snyder JW, Lambert JDC, Ogilby PR. Lifetime and diffusion of singlet oxygen in a cell. J Phys Chem B. 2005; 109: 8570-3.
113. Murotomi K, Umeno A, Sugino S, Yoshida Y. Quantitative kinetics of intracellular singlet oxygen generation using a fluorescence probe. Sci Rep. 2020; 10: 10616.
114. Sokolov VS, Batishchev OV, Akimov SA, Galimzyanov TR, Konstantinova AN, Malingriaux E, et al. Residence time of singlet oxygen in membranes. Sci Rep. 2018; 8: 14000.
115. Huang D, Cheng Y, Chen G, Zhao Y. 3D-printed Janus piezoelectric patches for sonodynamic bacteria elimination and wound healing. Research (Wash D C). 2023; 6: 0022.
116. Chen Y, Wang C, Zhang Z, Yu F, Wang Y, Ding J, et al. 3D-printed piezocatalytic hydrogels for effective antibacterial treatment of infected wounds. Int J Biol Macromol. 2024; 268: 131637.
117. Zhang S, Chen D, Gu Z, Luo H, Chen X, Fu Q. Ultrasound-triggered piezocatalytic conductive guar gum/PEDOT:PSS/BTO composite hydrogels for bacterial-infected skin wound healing. Nano TransMed. 2024; 3: 100035.
118. He Q, Yuan X, Rao Y, Heng X, Huang S, Wang Y, et al. Piezocatalytic H2-evolving gradient-porous antibacterial hydrogel foam for electrotherapy of infected pressure ulcers. Adv Funct Mater. 2026; 36: e31295.
119. Li X, Liu Y, Yang Q, Zhang W, Wang H, Zhang W, et al. Injectable piezoelectric hydrogel promotes tendon-bone healing via reshaping the electrophysiological microenvironment and M2 macrophage polarization. ACS Appl Mater Interfaces. 2025; 17: 22210-31.
120. Liu D, Wang X, Gao C, Zhang Z, Wang Q, Pei Y, et al. Biodegradable piezoelectric-conductive integrated hydrogel scaffold for repair of osteochondral defects. Adv Mater. 2024; 36: e2409400.
121. Devi SG, Thiyagarajan K, Amalan AJ, Pius A. Injectable, self-healing, ultrasonic-triggered piezocatalytic hydrogels for enhanced antibacterial efficacy and wound healing: an *in vitro* study. ACS Appl Eng Mater. 2025; 3: 2672-82.
122. Liu Y, Dzidotor G, Le TT, Vinikoor T, Morgan K, Curry EJ, et al. Exercise-induced piezoelectric stimulation for cartilage regeneration in rabbits. Sci Transl Med. 2022; 14: eabi7282.
123. Li X, Lin L, Zhu M, Li X, Yu J, Lu D, et al. Low-intensity focused ultrasound-activated piezoelectric gel bandage for diabetic wound repair and neuropathic pain relief. Nat Commun. 2026; 17: 4243.
124. Wang F, Guan S, Chen S, Qiu J, Liu X. An ultrasound-responsive hydrogel for diabetic wound electrotherapy based on interfacial ion/electron transfer. Adv Funct Mater. 2025; 35: 2510243.
125. Li L, Li Z, Yue M, Shao Y, Wang J, Song Y, et al. Mechano-iontronic hydrogels generating biomimetic endogenous bioelectricity for promoting cartilage regeneration. Adv Mater. 2026; 38: e14604.
126. Wang L, Yu Y, Zhao X, Zhang Z, Yuan X, Cao J, et al. A biocompatible self-powered piezoelectric poly(vinyl alcohol)-based hydrogel for diabetic wound repair. ACS Appl Mater Interfaces. 2022; 14: 46273-89.
127. Yao S, Chen T, Liu Z, Fan L, Xie Y, You S, et al. A dual-layer chitosan-based conductive hydrogel and piezoelectric film for ultrasound-driven wound repair and scar reduction. Carbohydr Polym. 2025; 370: 124305.
128. Liu X, Wan X, Sui B, Hu Q, Liu Z, Ding T, et al. Piezoelectric hydrogel for treatment of periodontitis through bioenergetic activation. Bioact Mater. 2024; 35: 346-61.
129. Li M, Hu X, Liu X, Zhao L, Zhao W, Li Y, et al. 3D bioprinted piezoelectric hydrogel synergized with LIPUS to promote bone regeneration. Mater Today Bio. 2025; 31: 101604.
130. Sun J, Zhang J, Yang L, Zhang C, Wang Y, Lei H, et al. Piezocatalytic strategy facilitates diabetic bone regeneration through high-performance anti-oxidative recycling. Chem Eng J. 2024; 480: 147931.
131. Xu W, Yu Y, Li K, Shen L, Liu X, Chen Y, et al. Surface-confined piezocatalysis inspired by ROS generation of mitochondria respiratory chain for ultrasound-driven noninvasive elimination of implant infection. ACS Nano. 2023; 17: 9415-28.
132. Blonsky MN, Zhuang HL, Singh AK, Hennig RG. Ab initio prediction of piezoelectricity in two-dimensional materials. ACS Nano. 2015; 9: 9885-91.
133. Ares P, Cea T, Holwill M, Wang YB, Roldán R, Guinea F, et al. Piezoelectricity in monolayer hexagonal boron nitride. Adv Mater. 2020; 32: e1905504.
134. Ong MT, Reed EJ. Engineered piezoelectricity in graphene. ACS Nano. 2012; 6: 1387-94.
135. Xue F, Zhang J, Hu W, Hsu WT, Han A, Leung SF, et al. Multi-direction piezoelectricity in mono- and multi-layered hexagonal α-In2Se3. ACS Nano. 2018; 12: 4976-83.
136. Zhu H, Wang Y, Xiao J, Liu M, Xiong S, Wong ZJ, et al. Observation of piezoelectricity in free-standing monolayer MoS2. Nat Nanotechnol. 2015; 10: 151-5.
137. Duerloo KAN, Ong MT, Reed EJ. Intrinsic piezoelectricity in two-dimensional materials. J Phys Chem Lett. 2012; 3: 2871-6.
138. Fei R, Li W, Li J, Yang L. Giant piezoelectricity of monolayer group IV monochalcogenides: SnSe, SnS, GeSe, and GeS. Appl Phys Lett. 2015; 107: 173104.
139. Wu W, Wang L, Li Y, Zhang F, Lin L, Niu S, et al. Piezoelectricity of single-atomic-layer MoS2 for energy conversion and piezotronics. Nature. 2014; 514: 470-4.
140. Chen C, Wang J, Xu J, Shi Q, Thong HC, Liu YX, et al. Synergistic defect-driven chemocatalysis and ultrasound-activated piezocatalysis by two-dimensional SnSe nanosheets. Nano Lett. 2025; 25: 10270-8.
141. Truong Hoang Q, Huynh KA, Nguyen Cao TG, Kang JH, Dang XN, Ravichandran V, et al. Piezocatalytic 2D WS2 nanosheets for ultrasound-triggered and mitochondria-targeted piezodynamic cancer therapy synergized with energy metabolism-targeted chemotherapy. Adv Mater. 2023; 35: e2300437.
142. Dong Y, Dong S, Liu B, Yu C, Liu J, Yang D, et al. 2D piezoelectric Bi2MoO6 nanoribbons for GSH-enhanced sonodynamic therapy. Adv Mater. 2021; 33: e2106838.
143. Zhang L, Yang T, Ding L, Chang M, Yin X, Chen Y, et al. Engineering 2D Bi4NbO8Br single crystalline nanosheets for piezoelectric and piezodynamic tumor nanotherapy. Chem Eng J. 2024; 484: 149445.
144. Li K, Wang S, Chen C, Xia L, Huang H, Feng W, et al. Endowing 1T'-ReS2 nanosheets with sonopiezoelectric property by theoretical-guided vacancy-manipulated Peierls distortion for tumor ferroptosis therapy. J Am Chem Soc. 2024; 146: 27779-93.
145. Chen Z, Sang L, Bian D, Liu Y, Bai Z. Piezo-catalytic immunotherapy: mechanisms and feasibility in cancer treatment. Theranostics. 2025; 15: 6236-52.
146. Qi G, Chen Z, Li J, Fu Z, Li Z, Jin Y. Electro-pyroptosis immunotherapy of cancer via endoplasmic reticulum-mitochondria crosstalk evoked by ultrasound-activated wireless electrostimulation. Adv Mater. 2026; 38: e73770.
147. Gao ML, Cao BL, Jiang LL, He HJ, Shi R, Yao XJ, et al. Engineering a carbolong nanoplatform for piezoelectric immunotherapy. ACS Nano. 2026; 20: 19577-89.
148. Du Y, Yang J, He F, Zhao X, Zhou J, Zang P, et al. Revealing the mutually enhanced mechanism of necroptosis and immunotherapy induced by defect engineering and piezoelectric effect. Adv Mater. 2024; 36: e2304322.
149. Tang Q, Sun S, Wang P, Sun L, Wang Y, Zhang L, et al. Genetically engineering cell membrane-coated BTO nanoparticles for MMP2-activated piezocatalysis-immunotherapy. Adv Mater. 2023; 35: e2300964.
150. Kong Y, Liu F, Ma B, Duan J, Yuan W, Sang Y, et al. Wireless localized electrical stimulation generated by an ultrasound-driven piezoelectric discharge regulates proinflammatory macrophage polarization. Adv Sci (Weinh). 2021; 8: 2100962.
151. Liu X, Xu W, Feng J, Wang Y, Li K, Chen Y, et al. Adoptive cell transfer of piezo-activated macrophage rescues immunosuppressed rodents from life-threating bacterial infections. Nat Commun. 2025; 16: 1363.
152. Du Y, Zhao X, He F, Gong H, Yang J, Wu L, et al. A vacancy-engineering ferroelectric nanomedicine for cuproptosis/apoptosis co-activated immunotherapy. Adv Mater. 2024; 36: e2403253.
153. Hao Z, He Y, Liu C, Xue W, Liu Z, Li A, et al. Piezoelectric catalytic activation of cGAS-STING pathway by Ga-based liquid metal nanoparticles for enhanced antitumor immunotherapy. Biomaterials. 2026; 327: 123745.
154. Song Y, Xu S, Zhang J, Zhang T, Wu R, Feng G, et al. Ultrasound-mediated piezocatalysis triggers NO release to augment targeted immunotherapy of pancreatic cancer. ACS Nano. 2025; 19: 32654-73.
155. Fan Y, Ye J, Kang Y, Niu G, Shi J, Yuan X, et al. Biomimetic piezoelectric nanomaterial-modified oral microrobots for targeted catalytic and immunotherapy of colorectal cancer. Sci Adv. 2024; 10: eadm9561.
156. Pu Y, Zhou B, Bing J, Wang L, Chen M, Shen Y, et al. Ultrasound-triggered and glycosylation inhibition-enhanced tumor piezocatalytic immunotherapy. Nat Commun. 2024; 15: 9023.
157. Cai L, Han F, Ding J, Zhou X, Shi T, Cheng F, et al. Biodegradable and piezoelectric Mn-doped hydroxyapatite for sonodynamic immunotherapy. ACS Nano. 2025; 19: 24067-77.
158. Zheng H, Lin H, Ke Y, Ma Y, Ge S, Yang F, et al. Piezoelectric-triggered ferroptosis for cancer therapy via cascade-enhanced immune response. Adv Healthc Mater. 2025; 14: e2501339.
159. Wang Y, Tang Q, Wu R, Yang S, Geng Z, He P, et al. Metformin-mediated fast charge-reversal nanohybrid for deep penetration piezocatalysis-augmented chemodynamic immunotherapy of cancer. ACS Nano. 2024; 18: 6314-32.
160. Li X, Yan R, Tan M, Kwok RTK, Sun J, Xiang H, et al. Facile access to piezoelectric polyamides by polyamidation of carboxylic acids and ynamides for potent tumor immunotherapy. Angew Chem Int Ed Engl. 2025; 64: e202424923.
161. Huang RH, Sobol NB, Younes A, Mamun T, Lewis JS, Ulijn RV, et al. Comparison of methods for surface modification of barium titanate nanoparticles for aqueous dispersibility: toward biomedical utilization of perovskite oxides. ACS Appl Mater Interfaces. 2020; 12: 51135-47.

162. Zhang X, Chen J, Min Y, Park GB, Shen X, Song S, et al. Metabolizable Bi2Se3 nanoplates: biodistribution, toxicity, and uses for cancer radiation therapy and imaging. Adv Funct Mater. 2014; 24: 1718-29.
163. Chen Z, Zhang W, Qu X, Zhang Y. Piezoelectric heterojunction-driven biomedical revolution: from construction principles to diagnostic and therapeutic applications. Theranostics. 2026; 16: 3136-72.
164. Choi HS, Liu W, Misra P, Tanaka E, Zimmer JP, Itty Ipe B, et al. Renal clearance of quantum dots. Nat Biotechnol. 2007; 25: 1165-70.
165. Wilhelm S, Tavares AJ, Dai Q, Ohta S, Audet J, Dvorak HF, et al. Analysis of nanoparticle delivery to tumours. Nat Rev Mater. 2016; 1: 16014.
166. Das R, Le TT, Schiff B, Chorsi MT, Park J, Lam P, et al. Biodegradable piezoelectric skin-wound scaffold. Biomaterials. 2023; 301: 122270.
167. Lu J, Hu S, Li W, Wang X, Mo X, Gong X, et al. A biodegradable and recyclable piezoelectric sensor based on a molecular ferroelectric embedded in a bacterial cellulose hydrogel. ACS Nano. 2022; 16: 3744-55.
168. Zhang Z, Wang Z, Li X, Zheng Y, Yang Z. Design and manufacturing of piezoelectric biomaterials for bioelectronics and biomedical applications. Chem Rev. 2025; 125: 9875-929.
169. Nain A, Chakraborty S, Barman SR, Gavit P, Indrakumar S, Agrawal A, et al. Progress in the development of piezoelectric biomaterials for tissue remodeling. Biomaterials. 2024; 307: 122528.
170. Faria M, Björnmalm M, Thurecht KJ, Kent SJ, Parton RG, Kavallaris M, et al. Minimum information reporting in bio-nano experimental literature. Nat Nanotechnol. 2018; 13: 777-85.
171. Percie du Sert N, Hurst V, Ahluwalia A, Alam S, Avey MT, Baker M, et al. The ARRIVE guidelines 2.0: updated guidelines for reporting animal research. PLoS Biol. 2020; 18: e3000410.
172. Bonvalot S, Rutkowski PL, Thariat J, Carrère S, Ducassou A, Sunyach MP, et al. NBTXR3, a first-in-class radioenhancer hafnium oxide nanoparticle, plus radiotherapy versus radiotherapy alone in patients with locally advanced soft-tissue sarcoma (Act.In.Sarc): a multicentre, phase 2-3, randomised, controlled trial. Lancet Oncol. 2019; 20: 1148-59.
173. Wang Y, Tang Q, Wu R, Sun S, Zhang J, Chen J, et al. Ultrasound-triggered piezocatalysis for selectively controlled NO gas and chemodrug release to enhance drug penetration in pancreatic cancer. ACS Nano. 2023; 17: 3557-73.
174. Deng R, Zhou H, Qin Q, Ding L, Song X, Chang M, et al. Palladium-catalyzed hydrogenation of black barium titanate for multienzyme-piezoelectric synergetic tumor therapy. Adv Mater. 2024; 36: e2307568.
175. Huang Y, Wan X, Su Q, Zhao C, Cao J, Yue Y, et al. Ultrasound-activated piezo-hot carriers trigger tandem catalysis coordinating cuproptosis-like bacterial death against implant infections. Nat Commun. 2024; 15: 1643.
176. Bößl F, Menzel VC, Chatzisymeon E, Comyn TP, Cowin P, Cobley AJ, et al. Effect of frequency and power on the piezocatalytic and sonochemical degradation of dyes in water. Chem Eng J Adv. 2023; 14: 100477.
177. ter Haar G, Shaw A, Pye S, Ward B, Bottomley F, Nolan R, et al. Guidance on reporting ultrasound exposure conditions for bio-effects studies. Ultrasound Med Biol. 2011; 37: 177-83.
178. Padilla F, ter Haar G. Recommendations for reporting therapeutic ultrasound treatment parameters. Ultrasound Med Biol. 2022; 48: 1299-308.
179. Murphy MP, Bayir H, Belousov V, Chang CJ, Davies KJA, Davies MJ, et al. Guidelines for measuring reactive oxygen species and oxidative damage in cells and *in vivo*. Nat Metab. 2022; 4: 651-62.
180. Kalyanaraman B, Darley-Usmar V, Davies KJA, Dennery PA, Forman HJ, Grisham MB, et al. Measuring reactive oxygen and nitrogen species with fluorescent probes: challenges and limitations. Free Radic Biol Med. 2012; 52: 1-6.
181. Zhao Y, Wang S, Ding Y, Zhang Z, Huang T, Zhang Y, et al. Piezotronic effect-augmented Cu2-xO-BaTiO3 sonosensitizers for multifunctional cancer dynamic therapy. ACS Nano. 2022; 16: 9304-16.
182. Wang Z, Berbille A, Feng Y, Li S, Zhu L, Tang W, et al. Contact-electro-catalysis for the degradation of organic pollutants using pristine dielectric powders. Nat Commun. 2022; 13: 130.
183. Wang Y, Xu Y, Dong S, Wang P, Chen W, Lu Z, et al. Ultrasonic activation of inert poly(tetrafluoroethylene) enables piezocatalytic generation of reactive oxygen species. Nat Commun. 2021; 12: 3508.
184. Burte AS, Nair A, Grabow LC, Dauenhauer PJ, Scott SL, Abdelrahman OA. CatTestHub: a benchmarking database of experimental heterogeneous catalysis for evaluating advanced materials. J Catal. 2025; 442: 115902.